Weierstraß-Institut
für Angewandte Analysis und Stochastik
Leibniz-Institut im Forschungsverbund Berlin e. V.

Preprint ISSN 2198-5855

Hybrid quantum-classical modeling of quantum dot devices

Markus Kantner, Markus Mittnenzweig, Thomas Koprucki

submitted: June 29, 2017

Weierstraß-Institut
Mohrenstr. 39
10117 Berlin
Germany
E-Mail: markus.kantner@wias-berlin.de
markus.mittnenzweig@wias-berlin.de
thomas.koprucki@wias-berlin.de

No. 2412
Berlin 2017

2010 *Mathematics Subject Classification.* 35Qxx, 81V65, 81V70, 81V80, 82D37, 82C10, 82C70.

2010 *Physics and Astronomy Classification Scheme.* 05.30.-d, 42.50.-p, 73.63.Kv, 85.30.De, 85.35.-p, 85.60.Bt.

Key words and phrases. device simulation, quantum dots, quantum-classical coupling, single-photon sources.

The work of M. K. has been support by the Deutsche Forschungsgemeinschaft (DFG) within the collaborative research center 787 *Semiconductor Nanophotonics* under grant B4. M. M. was supported by the ERC via AdG 267802 *AnaMultiScale*. The authors acknowledge valuable discussions with H.-J. Wünsche, U. Bandelow, D. Peschka and A. Mielke.

Edited by
Weierstraß-Institut für Angewandte Analysis und Stochastik (WIAS)
Leibniz-Institut im Forschungsverbund Berlin e. V.
Mohrenstraße 39
10117 Berlin
Germany

Fax: +49 30 20372-303
E-Mail: preprint@wias-berlin.de
World Wide Web: http://www.wias-berlin.de/

Hybrid quantum-classical modeling of quantum dot devices

Markus Kantner, Markus Mittnenzweig, Thomas Koprucki

Abstract

The design of electrically driven quantum dot devices for quantum optical applications asks for modeling approaches combining classical device physics with quantum mechanics. We connect the well-established fields of semi-classical semiconductor transport theory and the theory of open quantum systems to meet this requirement. By coupling the van Roosbroeck system with a quantum master equation in Lindblad form, we obtain a new hybrid quantum-classical modeling approach, which enables a comprehensive description of quantum dot devices on multiple scales: It allows the calculation of quantum optical figures of merit and the spatially resolved simulation of the current flow in realistic semiconductor device geometries in a unified way. We construct the interface between both theories in such a way, that the resulting hybrid system obeys the fundamental axioms of (non-)equilibrium thermodynamics. We show that our approach guarantees the conservation of charge, consistency with the thermodynamic equilibrium and the second law of thermodynamics. The feasibility of the approach is demonstrated by numerical simulations of an electrically driven single-photon source based on a single quantum dot in the stationary and transient operation regime.

1 Introduction

Semiconductor quantum dots (QDs) are zero-dimensional nanostructures which provide a discrete spectrum of electronic states due to the confinement of charge carriers in all spatial dimensions. Because of their tunable electro-optical properties and their easy integration into dielectric microcavities, QDs have attracted considerable attention in particular for applications in solid-state based optoelectronic devices [1–6]. These include e.g. highly efficient semiconductor micro- and nanolasers with a few or even a single QD as gain medium [7–11], semiconductor optical amplifiers [12], and quantum light sources such as single-photon emitters and sources of entangled photon pairs [13–17]. Applications comprise optical communication and quantum information processing [15, 16, 18], quantum cryptography [19], optical computing [20] and bio-chemical sensing [21].

Currently, quantum optics is making the leap from the lab to commercial applications. On this way, device engineers will need simulation tools, which combine classical device physics with models from quantum mechanics. The modeling and simulation of electrically driven semiconductor devices containing QDs constitutes a considerable challenge. On the one hand, modern optoelectronic devices increasingly employ quantum optical effects based on coherent light matter interaction, entanglement, photon counting statistics and non-classical correlations, which require a quantum mechanical description of the charge carriers and the optical field. In the last decades, light emitting devices based on a single or a few QDs have been successfully described by quantum master equations (QMEs) for the density matrix [8, 10, 22–26], which enable a detailed description of the dynamics of open quantum systems. On the other hand, the simulation of electrically driven devices requires a spatially resolved description of the current injection from the highly doped barriers and metal contacts into the optically active region containing the semiconductor QDs. The carrier transport problem is well described by

DOI 10.20347/WIAS.PREPRINT.2412 Berlin 2017

semi-classical transport models such as the van Roosbroeck system [27, 28], which describes the drift and diffusion of carriers within their self-consistently generated electric field. The van Roosbroeck system has been applied previously to QD devices, in particular to QD-based intermediate band solar cells [29, 30] and for the optimization of the current injection in single-photon sources [31].

Both fields, the theory of open quantum systems and the semi-classical semiconductor transport theory, are well developed and established for several decades. The scope of this paper is the self-consistent coupling of both theories in order to obtain a comprehensive description of QD based optoelectronic devices on multiple scales. Therefore, the interface connecting both systems will be constructed in such a way, that the resulting hybrid quantum-classical model guarantees the conservation of charge, consistency with the thermodynamic equilibrium and the second law of thermodynamics.

The paper is organized as follows: In Sec. 2 the model equations are introduced and the physical properties of the hybrid quantum-classical model are discussed. We present the structure of the coupling terms between both systems and investigate important features such as the conservation of charge. In Sec. 3 the consistency of the model equations with fundamental axioms of (non-)equilibrium thermodynamics is investigated. In particular, we construct the thermodynamic equilibrium solution by minimizing the grand potential of the coupled system and show that the hybrid model obeys the second law of thermodynamics. In Sec. 4 the approach is applied to the simulation of an electrically driven single-photon source based on a single QD. We study the stationary and transient excitation regime by numerical simulations and show how the model allows to compute the decisive quantum optical figures of merit along with the spatially resolved carrier transport characteristics. Finally, in Sec. 5 we give an outlook on possible improvements and extensions of the approach.

2 Model equations

We consider a hybrid quantum-classical model that self-consistently couples semi-classical transport theory to a kinetic equation for the quantum mechanical density matrix. The latter one is a QME in a Born-Markov and secular (rotating wave) approximation that describes the evolution of an open quantum system which interacts with its macroscopic environment [32–35]. In the following, the open quantum system is given by a single or a few QDs. Our approach is based on the assumption that the charge carriers can be separated into (free) continuum carriers and (bound) carriers confined to QDs, which is typically met for optoelectronic devices operating close to flat band conditions (weak electric fields) [36–38]. The model equations read

$$-\nabla \cdot \varepsilon \nabla \psi = q\left(p - n + C + Q\left(\rho\right)\right), \tag{1}$$

$$\partial_t n - \frac{1}{q}\nabla \cdot \mathbf{j}_n = -R - S_n\left(\rho\right), \tag{2}$$

$$\partial_t p + \frac{1}{q}\nabla \cdot \mathbf{j}_p = -R - S_p\left(\rho\right), \tag{3}$$

$$\frac{\mathrm{d}}{\mathrm{d}t}\rho = \mathcal{L}\left(\rho\right) = -\frac{i}{\hbar}\left[H, \rho\right] + \mathcal{D}\left(\rho\right) \tag{4}$$

on the domain $\Omega \subset \mathbb{R}^3$. The system (1)–(4) is subject to initial conditions and mixed boundary conditions modeling metal contacts, semiconductor-insulator interfaces and artificial boundaries [28, 39]. See Appendix A for the boundary conditions considered throughout this paper. A schematic illustration of the modeling approach is shown in Fig. 1.

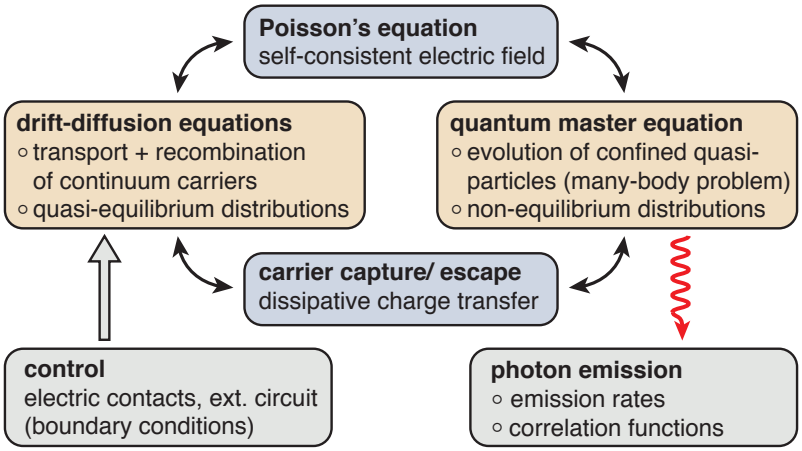

Figure 1: Schematic illustration of the hybrid quantum-classical modeling approach. A quantum system described by a QME is self-consistently coupled to the semi-classical transport equations for the freely roaming continuum carriers. Both (sub-)systems exchange charge carriers by capture and escape and interact via their self-consistently generated electric field.

2.1 Van Roosbroeck system

Eqns. (1)–(3) represent the standard van Roosbroeck system, extended by additional terms that constitute the coupling to the quantum system. Poisson's Eq. (1) describes the electrostatic potential ψ generated by the free electron and hole densities n and p, the (stationary) built-in doping profile C and the expectation value of the charge density $Q(\rho)$ of the carriers confined to the QDs. The dielectric permittivity of the semiconductor material is given by $\varepsilon = \varepsilon_0 \varepsilon_r$ and q denotes the elementary charge. The continuity equations (2)–(3) describe the flux of free electrons and holes in the presence of recombination and transitions between free and bound states. The (net-)recombination rate R includes several recombination channels such as Shockley-Read-Hall recombination, spontaneous emission and Auger recombination. Moreover, carriers can be scattered from the continuum to the QDs which is described by the (net-)capture rates S_n and S_p. The van Roosbroeck system must be augmented with additional state equations for the free carrier densities

$$n = N_c F_{1/2}\left(\beta\left(\mu_c - E_c + q\psi\right)\right), \tag{5a}$$

$$p = N_v F_{1/2}\left(\beta\left(E_v - q\psi - \mu_v\right)\right) \tag{5b}$$

and the electrical current densities

$$\mathbf{j}_n = \frac{1}{q}\sigma_n \nabla \mu_c, \tag{6a}$$

$$\mathbf{j}_p = \frac{1}{q}\sigma_p \nabla \mu_v. \tag{6b}$$

Here, N_c and N_v denote the effective density of states of the conduction and valence band and E_c and E_v are the respective band edge energies. The inverse temperature $\beta = (k_B T)^{-1}$ is considered as a fixed parameter and

$$F_\nu(\eta) = \frac{1}{\Gamma(\nu+1)} \int_0^\infty \mathrm{d}\xi \, \frac{\xi^\nu}{e^{\xi-\eta}+1}$$

is the Fermi–Dirac integral of order ν. The state equations (5) describe thermalized carrier ensembles in a quasi-equilibrium distribution, where the quasi-Fermi energies of the conduction band μ_c and the

valence band μ_v parametrize the deviation from the global thermodynamic equilibrium. In accordance with linear irreversible thermodynamics, the current densities are driven by the gradients of the quasi-Fermi energies [40, 41]. The electrical conductivities $\sigma_n = qM_n n$, $\sigma_p = qM_p p$ are products of the free carrier densities and the carrier mobilities $M_{n/p}$ [28].

2.2 Quantum master equation

The state of the quantum system is described by the density matrix ρ, which is subject to the QME (4). Here, the open quantum system represents a many-body problem describing the charge carriers confined to QDs and possibly further quasi-particles, e.g. cavity photons, phonons or exciton-polaritons (dressed states).

The Hamiltonian in Eq. (4) takes the form

$$H = H_0 + H_I,$$

where H_0 describes the single-particle energies of the confined electrons and holes (and possibly additional particle species). The interaction Hamiltonian H_I is assumed to commute with the charge number operator

$$N = n_e - n_h \tag{7}$$

(n_e and n_h are the number operators of the bound electrons and holes) such that the Hamiltonian part of the evolution conserves the net charge

$$[H, N] = 0. \tag{8}$$

This imposes only a weak restriction on H_I and allows e.g. for Coulomb interaction between the confined carriers (configuration interaction) as well as coherent light-matter interaction.

The non-Hamiltonian part of the evolution of the quantum system is modeled by a dissipator of the form

$$\mathcal{D}(\rho) = \sum_\alpha \Big(\gamma_\alpha \big(A_\alpha \rho A_\alpha^\dagger - \frac{1}{2} \{ A_\alpha^\dagger A_\alpha, \rho \} \big) + \hat{\gamma}_\alpha \big(A_\alpha^\dagger \rho A_\alpha - \frac{1}{2} \{ A_\alpha A_\alpha^\dagger, \rho \} \big) \Big), \tag{9}$$

which is a superoperator in *Lindblad form* acting on the density matrix. The symbol $\{A, B\} = AB + BA$ denotes the anti-commutator. The dissipator accounts for various irreversible interactions (indexed by α) of the open system with its macroscopic environment. In this paper, the environment of the quantum system is the spatio-temporally resolved free electron-hole plasma, which itself is subject to the van Roosbroeck system (1)–(3). A QME in Lindblad form ensures the preservation of trace, hermiticity and (complete) positivity of the density matrix [33, 34]. The operators A_α represent the *quantum jump operators*, which are projectors between different eigenstates of H. Following the standard construction of a Lindblad-QME for a weak system-reservoir interaction [32, 35] (extended to the case of variable charge number here), we require the jump operators to satisfy

$$[H, A_\alpha] = -\hbar\omega_\alpha A_\alpha, \tag{10a}$$
$$[N, A_\alpha] = -\ell_\alpha A_\alpha, \tag{10b}$$

where $\hbar\omega_\alpha$ denotes the transition energy and $\ell_\alpha \in \mathbb{Z}$ quantifies the charge transfer of the interaction described by A_α. We assume a decomposition of the dissipator into several channels

$$\mathcal{D}(\rho) = \mathcal{D}_e(\rho) + \mathcal{D}_h(\rho) + \mathcal{D}_0(\rho) \tag{11}$$

(with α in Eq. (9) running over disjoint index sets I_e, I_h and I_0). Here, $\mathcal{D}_e(\rho)$ and $\mathcal{D}_h(\rho)$ are dissipators which can change the charge of the quantum system (by capture and escape of electrons and holes), whereas the processes described by $\mathcal{D}_0(\rho)$ leave the charge invariant (e.g. spontaneous emission, photon absorption, intraband carrier relaxation, outcoupling of cavity photons, simultaneous capture of electrons and holes), i.e. it holds

$$\operatorname{tr}(N\mathcal{D}_0(\rho)) = 0. \tag{12}$$

Throughout this paper, we restrict ourselves to dissipators which satisfy the quantum detailed balance principle with respect to the thermodynamic equilibrium [42, 43]. Details on this will be discussed in Sec. 3.3.

2.3 Macroscopic coupling terms and charge conservation

By taking the time derivative of Poisson's Eq. (1) and using Eq. (2)–(3), we obtain the continuity equation

$$\nabla \cdot \mathbf{j}_{\text{tot}} = q(\partial_t Q - S_p + S_n)$$

for the total current density $\mathbf{j}_{\text{tot}} = \mathbf{j}_n + \mathbf{j}_p + \partial_t \mathbf{D}$. Besides the flux of charge carriers, it also includes the displacement current density $\partial_t \mathbf{D} = -\varepsilon \partial_t \nabla \psi$. For the sake of simplicity, we consider a quantum system comprising only a single QD. The generalization of the approach outlined below to the case of multiple QDs is straightforward. We approximate the electric charge density of the QD by the expectation value of the (net-)charge operator

$$Q(\rho) = -w(\mathbf{r}) \operatorname{tr}(N\rho), \tag{13}$$

where w models the spatial profile of the captured carriers, which is assumed to be identical for all carriers. The function w is normalized such that $\int_\Omega \mathrm{d}^3 r\, w(\mathbf{r}) = 1$. The spatial profile w replaces the absolute squares of the many-body wave functions of the bound carriers. The actual spatial distributions of the confined carriers differ only on a small length scale, which can be safely neglected in the simulation of macroscopic charge transport. In the form of Eq. (13), the model accounts for long range electrostatic correlations induced by the confined carriers.

Using Eqns. (4), (8), (11) and (12), the time derivative of Eq. (13) is obtained as

$$\partial_t Q = -w(\mathbf{r}) \operatorname{tr}(N\mathcal{D}_e(\rho)) - w(\mathbf{r}) \operatorname{tr}(N\mathcal{D}_h(\rho)).$$

Consequently, in order to ensure local charge conservation $\nabla \cdot \mathbf{j}_{\text{tot}} = 0$, the (net-)capture rates appearing in the carrier transport equations (2) and (3) are identified as

$$S_n = +w(\mathbf{r}) \operatorname{tr}(N\mathcal{D}_e(\rho)), \tag{14a}$$

$$S_p = -w(\mathbf{r}) \operatorname{tr}(N\mathcal{D}_h(\rho)). \tag{14b}$$

The (net-)capture rates $S_{n/p}$ contain all microscopic capture processes connected with transitions between the various multi-particle configurations of the QD.

For different choices of $Q(\rho)$, e.g. different localization profiles of captured electrons and holes $Q(\rho) = w_h(\mathbf{r}) \operatorname{tr}(n_h\rho) - w_e(\mathbf{r}) \operatorname{tr}(n_e\rho)$ (with $w_{e/h}$ normalized), the property of strict local charge conservation is lost in general. However, the violation of local charge conservation is restricted to a small region $\nabla \cdot \mathbf{j}_{\text{tot}} \propto (w_e(\mathbf{r}) - w_h(\mathbf{r}))$ and is preserved globally, i.e. it holds $\int_\Omega \mathrm{d}^3 r\, \nabla \cdot \mathbf{j}_{\text{tot}} = 0$.

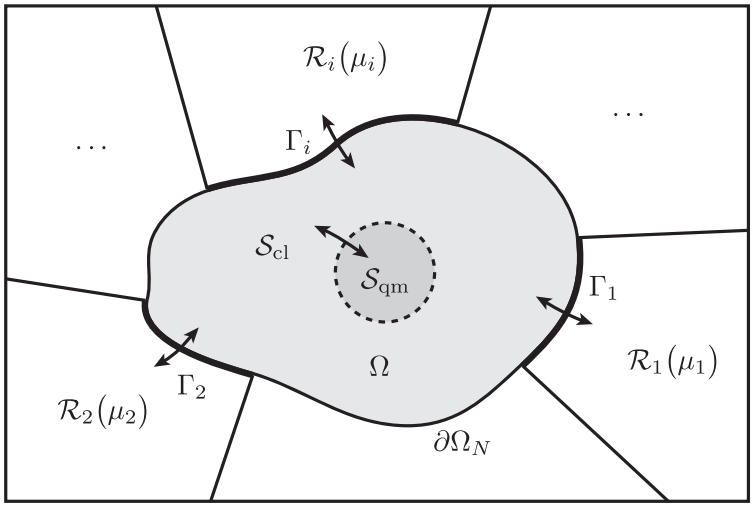

Figure 2: Sketch of the system $\mathcal{S}$, its surrounding reservoirs and boundaries for charge and energy exchange. The system $\mathcal{S}$ consists of a macroscopic subsystem $\mathcal{S}_{\mathsf{cl}}$ and a microscopic subsystem $\mathcal{S}_{\mathsf{qm}}$ in the interior of the domain Ω. The reservoirs $\mathcal{R}_{i\geq 1}$ denote electric contacts. The crystal lattice $\mathcal{R}_0$ spatially overlaps with $\mathcal{S}$ and is therefore not shown. Across the artificial boundaries labeled with $\partial\Omega_N$ neither energy nor charge exchange is admitted.

3 Thermodynamics

In the recent years, the on-going miniaturization of (quantum) electronic devices has enabled the investigation of thermodynamical laws on the nanoscale. This has lead to the emergence of the novel field of *quantum thermodynamics* [44–47]. Experiments and theory indicate that the fundamental thermodynamical laws also hold in the quantum regime [48, 49] and therefore we view thermodynamic consistency as a crucial feature for any hybrid quantum-classical model.

In this section we discuss the thermodynamic properties of the hybrid model system (1)–(4). At first, this concerns a consideration of the energy, charge and entropy balance between the system and its reservoirs. Second, the thermodynamic equilibrium solution of the hybrid system will be constructed by minimizing its grand potential. Moreover, we formulate a relation between the microscopic transition rates satisfying the quantum detailed balance condition. Finally, the hybrid quantum-classical model (1)–(4) is shown to have a non-negative entropy production rate, which we interpret as consistency with the second law of thermodynamics.

3.1 Energy, charge and entropy balance

We consider an open system $\mathcal{S}$, which itself consists of a classical and a quantum-mechanical subsystem $\mathcal{S} = \mathcal{S}_{\mathsf{cl}} \cup \mathcal{S}_{\mathsf{qm}}$, that is in contact with several reservoirs $\mathcal{R} = \bigcup_i \mathcal{R}_i$ as illustrated in Fig. 2. The system $\mathcal{S}$ can exchange energy and charge carriers with the reservoirs. The combined system $\mathcal{S} \cup \mathcal{R}$ is assumed to be isolated. The reservoir $\mathcal{R}_0$ subsumes the crystal lattice as well as the surrounding radiation field, which are characterized by the fixed background temperature T. The reservoirs $\mathcal{R}_{i\geq 1}$ model the electric contacts at the boundary of the device. They are described by their chemical potentials μ_i (or applied voltages), which are external control parameters.

The total change of entropy is given by

$$\Delta S_{\text{tot}} = \Delta S_{\mathcal{S}} + \Delta S_{\mathcal{R}} \geq 0,$$

and the conservation of the total internal energy and charge is expressed as

$$\begin{aligned}\Delta U &= \Delta U_{\mathcal{S}} + \Delta U_{\mathcal{R}} = 0,\\ \Delta N &= \Delta N_{\mathcal{S}} + \Delta N_{\mathcal{R}} = 0.\end{aligned}$$

The reservoir $\mathcal{R}_0$ can exchange only energy with $\mathcal{S}$, hence its change of entropy is given by $\Delta S_{\mathcal{R}_0} = \frac{1}{T}\Delta U_{\mathcal{R}_0}$. For the contacts $\mathcal{R}_{i\geq 1}$, also charge transfer is possible such that $\Delta S_{\mathcal{R}_i} = \frac{1}{T}\Delta U_{\mathcal{R}_i} - \frac{\mu_i}{T}\Delta N_{\mathcal{R}_i}$. Using the conservation laws state above, we obtain

$$\Delta S_{\text{tot}} = \Delta S_{\mathcal{S}} - \frac{1}{T}\Delta U_{\mathcal{S}} - \sum_{i\geq 1}\frac{\mu_i}{T}\Delta N_{\mathcal{R}_i},$$

where $\Delta N_{\mathcal{R}_i}$ is just the negative charge flow across the boundary Γ_i. Using

$$\lim_{\Delta t\to 0}\frac{\Delta N_{\mathcal{R}_i}}{\Delta t} = \frac{\mathrm{d}N_{\mathcal{R}_i}}{\mathrm{d}t} = -\frac{1}{q}\int_{\Gamma_i}\mathrm{d}\mathbf{A}\cdot\left(\mathbf{j}_n + \mathbf{j}_p\right),$$

we obtain the entropy production rate

$$\frac{\mathrm{d}S_{\text{tot}}}{\mathrm{d}t} = -\frac{1}{T}\frac{\mathrm{d}F_{\mathcal{S}}}{\mathrm{d}t} + \sum_{i\geq 1}\frac{\mu_i}{qT}\int_{\Gamma_i}\mathrm{d}\mathbf{A}\cdot\left(\mathbf{j}_n + \mathbf{j}_p\right), \tag{15}$$

where $F_{\mathcal{S}} = U_{\mathcal{S}} - TS_{\mathcal{S}}$ denotes the free energy of the system $\mathcal{S}$. In Sec. 3.4 it will be shown, that the entropy production rate is indeed always positive for the hybrid model (1)–(4). Under chemical equilibrium boundary conditions (all reservoirs $\mathcal{R}_{i\geq 1}$ have the same chemical potential $\mu_i = \mu_{\text{eq}}$), the above expression simplifies further. Exploiting the conservation of total charge, one obtains

$$\left.\frac{\mathrm{d}S_{\text{tot}}}{\mathrm{d}t}\right|_{\text{eq}} = -\frac{1}{T}\frac{\mathrm{d}\Omega_{\mathcal{S}}}{\mathrm{d}t} \tag{16}$$

with the grand potential $\Omega_{\mathcal{S}} = U_{\mathcal{S}} - TS_{\mathcal{S}} - \mu_{\text{eq}}N_{\mathcal{S}}$. Thus, the grand potential $\Omega_{\mathcal{S}}$ is a Lyapunov function for the irreversible relaxation of $\mathcal{S}$ into the thermodynamic equilibrium.

3.2 Thermodynamic equilibrium

According to Eq. (16), the thermodynamic equilibrium solution of (1)–(4) can be constructed by minimizing the grand potential $\Omega_{\mathcal{S}}$. Since we assume only a weak coupling between the quantum system and its macroscopic environment, the total entropy, total internal energy and total charge number are given by sums of the classical and the quantum mechanical contribution

$$S\left(n,p,\rho\right) = S_{\text{cl}}\left(n,p\right) + S_{\text{qm}}\left(\rho\right), \tag{17a}$$

$$U\left(n,p,\rho\right) = U_{\text{cl}}\left(n,p\right) + U_{\text{qm}}\left(\rho\right) + U_{\psi}\left(p - n + Q\left(\rho\right)\right), \tag{17b}$$

$$N\left(n,p,\rho\right) = N_{\text{cl}}\left(n,p\right) + N_{\text{qm}}\left(\rho\right). \tag{17c}$$

Here also the energy contribution U_ψ of the electrostatic field is taken into account. The extensive thermodynamic quantities of the macroscopic system are expressed via volume densities

$$\begin{aligned} S_{\mathsf{cl}}(n,p) &= \int_\Omega \mathrm{d}^3 r\, s_{\mathsf{cl}}(n,p)\,, \\ U_{\mathsf{cl}}(n,p) &= \int_\Omega \mathrm{d}^3 r\, u_{\mathsf{cl}}(n,p)\,, \\ N_{\mathsf{cl}}(n,p) &= \int_\Omega \mathrm{d}^3 r\ (n-p) \end{aligned}$$

with the entropy density s_{cl} and the internal energy density u_{cl}. We consider the continuum carriers to be in a *local thermodynamic equilibrium* [40]. Hence, the internal energy density and the entropy density can be expressed as functions of the local carrier density

$$\begin{aligned} s_{\mathsf{cl}}(n,p) = &-k_B\left(nF_{1/2}^{-1}\left(\frac{n}{N_c}\right) - \frac{5}{2}N_cF_{3/2}\left(F_{1/2}^{-1}\left(\frac{n}{N_c}\right)\right)\right) \\ &- k_B\left(pF_{1/2}^{-1}\left(\frac{p}{N_v}\right) - \frac{5}{2}N_vF_{3/2}\left(F_{1/2}^{-1}\left(\frac{p}{N_v}\right)\right)\right), \end{aligned} \tag{18a}$$

$$\begin{aligned} u_{\mathsf{cl}}(n,p) = &\frac{3}{2}k_BTN_cF_{3/2}\left(F_{1/2}^{-1}\left(\frac{n}{N_c}\right)\right) + E_cn \\ &+ \frac{3}{2}k_BTN_vF_{3/2}\left(F_{1/2}^{-1}\left(\frac{p}{N_v}\right)\right) - E_vp. \end{aligned} \tag{18b}$$

The above relations are obtained for the quasi-free electron and hole gas with parabolic energy dispersion and Fermi–Dirac statistics in three dimensions [50]. The contributions of the quantum system are given by the von Neumann entropy and the expectation values of the Hamiltonian H and the charge number operator N

$$S_{\mathsf{qm}} = -k_B\mathrm{tr}\left(\rho\log\rho\right), \tag{19a}$$

$$U_{\mathsf{qm}} = \mathrm{tr}\left(H\rho\right), \tag{19b}$$

$$N_{\mathsf{qm}} = \mathrm{tr}\left(N\rho\right). \tag{19c}$$

The free carriers interact via their self-consistently generated electrostatic field, which yields the contribution U_ψ to the internal energy. It is convenient to decompose the total electrostatic potential into $\psi = \psi_{\mathsf{int}} + \psi_{\mathsf{ext}}$, where the internal field $\psi_{\mathsf{int}} = \psi_{\mathsf{int}}(\rho_{\mathsf{int}})$ is generated by the total internal carrier density

$$\rho_{\mathsf{int}} = p - n + Q(\rho)\,,$$

whereas the external field ψ_{ext} arises from the built-in doping profile and voltages applied at the electric contacts. Then, the field energy can be written as [51]

$$U_\psi(\rho_{\mathsf{int}}) = \frac{1}{2}\int_\Omega \mathrm{d}^3 r\,\varepsilon\left|\nabla\psi_{\mathsf{int}}(\rho_{\mathsf{int}})\right|^2 + q\int_\Omega \mathrm{d}^3 r\,\rho_{\mathsf{int}}\psi_{\mathsf{ext}} + \frac{1}{2}\frac{\varepsilon_{\mathsf{ox}}}{d_{\mathsf{ox}}}\int_{\Gamma_G}\mathrm{d}A\,\psi_{\mathsf{int}}^2(\rho_{\mathsf{int}})\,. \tag{20}$$

The last term describes Gate contacts, which may occur in certain devices. See the Appendix B for details.

Assuming the charge density of the quantum system as stated in Eq. (13), and finally minimizing the grand potential $\Omega_{\mathcal{S}}$ under the constraint $\mathrm{tr}\left(\rho\right) = 1$, we obtain the equilibrium free carrier densities as

$$\begin{aligned} n_{\mathsf{eq}} &= N_cF_{1/2}\left(\beta\left(\mu_{\mathsf{eq}} - E_c + q\psi_{\mathsf{eq}}\right)\right), \\ p_{\mathsf{eq}} &= N_vF_{1/2}\left(\beta\left(E_v - q\psi_{\mathsf{eq}} - \mu_{\mathsf{eq}}\right)\right) \end{aligned}$$

and the equilibrium density matrix

$$\rho_{\mathsf{eq}} = \frac{1}{Z} e^{-\beta\left(H - \left(\mu_{\mathsf{eq}} + q\langle\psi_{\mathsf{eq}}\rangle_w\right)N\right)}. \tag{21}$$

Here, $Z = \mathrm{tr}\left(\exp\left(-\beta\left(H - \left(\mu_{\mathsf{eq}} + q\left\langle\psi_{\mathsf{eq}}\right\rangle_w\right)N\right)\right)\right)$ represents the grand canonical partition function,

$$\left\langle\psi\right\rangle_w = \int_\Omega \mathrm{d}^3 r\, w\left(\mathbf{r}\right)\psi\left(\mathbf{r}\right) \tag{22}$$

is the averaged electrostatic potential in the vicinity of the QD and the *built-in potential* ψ_{eq} solves Eq. (1) with the right hand side $q\left(p_{\mathsf{eq}} - n_{\mathsf{eq}} + C + Q\left(\rho_{\mathsf{eq}}\right)\right)$ at equilibrium boundary conditions. The equilibrium density matrix is a grand canonical ensemble, which contains a contribution from the electrostatic potential due to the electrostatic interaction with the macroscopic system. The field contribution in Eq. (21) appears as a spatial average using the localization profile w of the confined carriers as a weighting function, see Eq. (22). This is a remarkable result, which indicates that the quantum system interacts only with its spatially averaged macroscopic environment. We emphasize that this is a direct consequence of the ansatz Eq. (13) and the variation of Eq. (20) with respect to n, p and ρ. See Appendix B for details.

In the following, the concept of a non-local interaction of the quantum system with its spatially averaged macroscopic environment will be extended to non-equilibrium situations.

3.3 Microscopic transition rates and the quantum detailed balance condition

We assume the microscopic transition rates in the dissipator (9) to be functions of the spatially averaged macroscopic potentials

$$\begin{aligned}\gamma_\alpha &= \gamma_\alpha\left(\left\langle\mu_c\right\rangle_w, \left\langle\mu_v\right\rangle_w, \left\langle\psi\right\rangle_w\right),\\ \hat{\gamma}_\alpha &= \hat{\gamma}_\alpha\left(\left\langle\mu_c\right\rangle_w, \left\langle\mu_v\right\rangle_w, \left\langle\psi\right\rangle_w\right),\end{aligned}$$

where $\left\langle\cdot\right\rangle_w$ denotes the spatial average according to Eq. (22). The quantum detailed balance condition requires the dissipator to vanish in equilibrium. Hence, the condition

$$0 \overset{!}{=} \mathcal{D}_\alpha\left(\rho_{\mathsf{eq}}\right) = \gamma_\alpha^{\mathsf{eq}}\left(A_\alpha\rho_{\mathsf{eq}}A_\alpha^\dagger - \frac{1}{2}\left\{A_\alpha^\dagger A_\alpha, \rho_{\mathsf{eq}}\right\}\right) + \hat{\gamma}_\alpha^{\mathsf{eq}}\left(A_\alpha^\dagger\rho_{\mathsf{eq}}A_\alpha - \frac{1}{2}\left\{A_\alpha A_\alpha^\dagger, \rho_{\mathsf{eq}}\right\}\right)$$

can be used to derive a relation between the equilibrium transition rates $\gamma_\alpha^{\mathsf{eq}} = \gamma_\alpha\left(\mu_{\mathsf{eq}}, \mu_{\mathsf{eq}}, \left\langle\psi_{\mathsf{eq}}\right\rangle_w\right)$ and $\hat{\gamma}_\alpha^{\mathsf{eq}}$. From Eq. (10), one obtains for any $\lambda \in \mathbb{R}$

$$\begin{aligned}e^{\lambda H}A_\alpha e^{-\lambda H} &= e^{-\lambda\hbar\omega_\alpha}A_\alpha,\\ e^{\lambda N}A_\alpha e^{-\lambda N} &= e^{-\lambda\ell_\alpha}A_\alpha,\end{aligned}$$

which implies

$$\begin{aligned}A_\alpha\rho_{\mathsf{eq}} &= e^{-\beta\left(\hbar\omega_\alpha - \left(\mu_{\mathsf{eq}} + q\langle\psi_{\mathsf{eq}}\rangle_w\right)\ell_\alpha\right)}\rho_{\mathsf{eq}}A_\alpha,\\ A_\alpha^\dagger\rho_{\mathsf{eq}} &= e^{+\beta\left(\hbar\omega_\alpha - \left(\mu_{\mathsf{eq}} + q\langle\psi_{\mathsf{eq}}\rangle_w\right)\ell_\alpha\right)}\rho_{\mathsf{eq}}A_\alpha^\dagger.\end{aligned}$$

Subsequently, one obtains

$$\begin{aligned}\mathcal{D}_\alpha\left(\rho_{\mathsf{eq}}\right) = &\left(\gamma_\alpha^{\mathsf{eq}} - \hat{\gamma}_\alpha^{\mathsf{eq}}e^{+\beta\left(\hbar\omega_\alpha - \left(\mu_{\mathsf{eq}} + q\langle\psi_{\mathsf{eq}}\rangle_w\right)\ell_\alpha\right)}\right)\times\\ &\times\left(A_\alpha\rho_{\mathsf{eq}}A_\alpha^\dagger - e^{-\beta\left(\hbar\omega_\alpha - \left(\mu_{\mathsf{eq}} + q\langle\psi_{\mathsf{eq}}\rangle_w\right)\ell_\alpha\right)}A_\alpha^\dagger\rho_{\mathsf{eq}}A_\alpha\right),\end{aligned}$$

which yields the desired relation between $\gamma_\alpha^{\mathsf{eq}}$ and $\hat{\gamma}_\alpha^{\mathsf{eq}}$:

$$\hat{\gamma}_\alpha^{\mathsf{eq}} = \gamma_\alpha^{\mathsf{eq}} e^{-\beta\left(\hbar\omega_\alpha - \left(\mu_{\mathsf{eq}} + q\langle\psi_{\mathsf{eq}}\rangle_w\right)\ell_\alpha\right)}.$$

This agrees with the relation imposed by the Kubo-Martin-Schwinger (KMS) condition on the equilibrium reservoir correlation functions [35, 43]. Since throughout this paper we consider only thermalized reservoirs, we extend the above relation to non-equilibrium situations

$$\hat{\gamma}_\alpha\left(\langle\mu_c\rangle_w, \langle\mu_v\rangle_w, \langle\psi\rangle_w\right) = e^{-\beta\left(\hbar\omega_\alpha - \left(\langle\mu_\alpha\rangle_w + q\langle\psi\rangle_w\right)\ell_\alpha\right)}\gamma_\alpha\left(\langle\mu_c\rangle_w, \langle\mu_v\rangle_w, \langle\psi\rangle_w\right) \tag{23}$$

with $\mu_{\alpha\in I_e} = \mu_c$ and $\mu_{\alpha\in I_h} = \mu_v$. For charge-conserving processes we require $\ell_{\alpha\in I_0} = 0$, single electron-capture processes are described by $\ell_{\alpha\in I_e} = -1$ and for single hole-capture processes it holds $\ell_{\alpha\in I_h} = +1$.

Thus, supposing Eq. (23), the hybrid model obeys the quantum detailed balance condition for any model of the transition rate $\gamma_\alpha\left(\langle\mu_c\rangle_w, \langle\mu_v\rangle_w, \langle\psi\rangle_w\right) \geq 0$ that is non-negative. Physically, the latter one must represent a parametrization of a microscopically derived transition rate (using Fermi's Golden Rule [52]) in terms of the averaged macroscopic potentials. In particular, this enables the inclusion of microscopically calculated capture rates as presented e.g. in Refs. [53–58].

3.4 Entropy production and the second law of thermodynamics

From Eq. (15) we obtain the entropy production rate as (see Appendix C for the derivation)

$$\begin{aligned}\frac{\mathrm{d}S_{\mathsf{tot}}}{\mathrm{d}t} = &\frac{1}{T}\int_\Omega \mathrm{d}^3r\ \left(\mu_c - \mu_v\right) R \\ &+ \frac{1}{qT}\int_\Omega \mathrm{d}^3r\ \left(\mathbf{j}_n\cdot\nabla\mu_c + \mathbf{j}_p\cdot\nabla\mu_v\right) \\ &- k_B\mathrm{tr}\left(\left(\beta H + \log\rho\right)\mathcal{D}_0\left(\rho\right)\right) \\ &- k_B\mathrm{tr}\left(\left(\beta\left(H - \mu_c^{\mathsf{eff}}N\right) + \log\rho\right)\mathcal{D}_e\left(\rho\right)\right) \\ &- k_B\mathrm{tr}\left(\left(\beta\left(H - \mu_v^{\mathsf{eff}}N\right) + \log\rho\right)\mathcal{D}_h\left(\rho\right)\right)\end{aligned} \tag{24}$$

with $\mu_{c/v}^{\mathsf{eff}} = \left\langle\mu_{c/v}\right\rangle_w + q\left\langle\psi\right\rangle_w$. The first two lines are the entropy production rate of the van Roosbroeck system [59] and the third line describes the entropy production rate arising from internal processes within the open quantum system. The fourth and fifth line represent the contributions arising from the coupling of the macroscopic and the quantum mechanical subsystem via capture and escape. All terms are products of abstract thermodynamic forces and their corresponding fluxes, which is in agreement with the general theory of linear irreversible thermodynamics [40, 60]. All individual lines of Eq. (24) are non-negative and therefore

$$\frac{\mathrm{d}S_{\mathsf{tot}}}{\mathrm{d}t} \geq 0,$$

where the equality holds only in the case of thermodynamic equilibrium. A proof is given in the Appendix D. This results relies on the specific coupling imposed in the previous sections, which involves the spatially averaged macroscopic potentials. We emphasize, that if e.g. averaged carrier densities were used instead, a non-negative entropy production rate could not be guaranteed in general. Finally, we conclude that our hybrid quantum-classical modeling approach is consistent with the second law of thermodynamics.

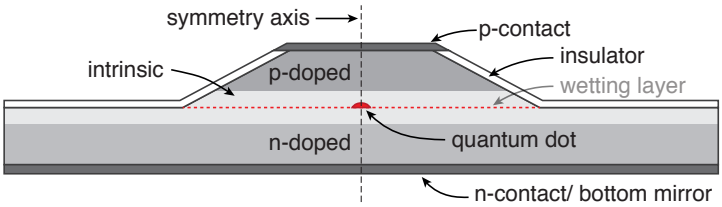

Figure 3: Cross section of the example device considered in the numerical simulations: A single QD is placed on the symmetry axis within the center of the intrinsic zone of a cylindrical p-i-n diode with etched mesa structure on top. The bottom mirror leads to a directed emission in vertical direction. Due to the lack of a top mirror, the device represents a leaky photonic cavity with low Q factor. The device has electric contacts at the top and the bottom facets.

Our approach can also be interpreted as a damped Hamiltonian system in the framework of GENERIC (*general equation for the non-equilibrium reversible-irreversible coupling*) [61], which automatically ensures a non-negative entropy production rate and the existence of an unique thermodynamic equilibrium. It can be applied to a wide range of physical problems [62–64].

4 Application to electrically driven single-photon sources

In this section we demonstrate the capability of our approach by the numerical simulation of an electrically driven single-photon source based on a p-i-n diode including a single QD. Such devices have been shown to act as single-photon emitters and are promising candidates for applications in quantum communication networks [65–69].

4.1 Model specification

The model equations are described in Sec. 2 and 3. For the hybrid system (1)–(4), we have to specify the Hamiltonian H as well as the quantum jump operators A_α and the transition rates γ_α, which constitute the dissipative interactions with the macroscopic environment. In particular, they need to satisfy the conditions (8) and (12) that guarantee charge conservation and the eigenoperator relations (10).

4.1.1 Hamiltonian

We consider a single QD embedded in a very leaky dielectric cavity with low Q factor, which is sketched in Fig. 3. In such devices, the light-matter interaction is governed by spontaneous emission and thus can be described by a Lindblad dissipator. Hence, we can model the quantum system by a purely electronic Hamiltonian. We aim for a description of the electronic QD states in terms of many-body states covering single particle states, excitons, trions and the biexciton as shown in Fig. 4(a). We assume a single one-particle level (ground state) for the electrons and holes each, labeled by ε_c and ε_v, respectively. The Hamiltonian

$$H = H_0 + H_I$$

contains the single-particle contributions

$$H_0 = \sum_\sigma \varepsilon_c e_\sigma^\dagger e_\sigma - \sum_\sigma \varepsilon_v h_\sigma^\dagger h_\sigma$$

and their Coulomb interaction

$$H_I = \frac{1}{2}\sum_{\sigma,\sigma'}\left(V_{c,c}e^\dagger_\sigma e^\dagger_{\sigma'}e_{\sigma'}e_\sigma + V_{v,v}h^\dagger_\sigma h^\dagger_{\sigma'}h_{\sigma'}h_\sigma - 2V_{c,v}e^\dagger_\sigma h^\dagger_{\sigma'}h_{\sigma'}e_\sigma\right).$$

The operators $e^\dagger_\sigma$ (e_σ) and $h^\dagger_\sigma$ (h_σ) create (annihilate) an electron or hole with total angular momentum quantum number in z-direction σ. We consider a single valence band describing heavy holes with a pseudo spin $\pm 3/2$ indicated by $\{\Uparrow, \Downarrow\}$. Here, only direct (Hartree-like) Coulomb matrix elements $V_{i,j} = V_{i,j,j,i}$ occur, which are of the order of several tens of meV (see Appendix F). The creation and annihilation operators obey the fermionic anti-commutator relations $\{e_\sigma, e^\dagger_{\sigma'}\} = \{h_\sigma, h^\dagger_{\sigma'}\} = \delta_{\sigma,\sigma'}$, $\{e_\sigma, e_{\sigma'}\} = \{h_\sigma, h_{\sigma'}\} = 0$ and $[e_\sigma, h_{\sigma'}] = 0$. The single-particle energy levels and the Coulomb matrix elements are obtained from Schödinger's equation with an effective confinement potential for InGaAs-QDs [54, 56, 70]. With the number operators $n_{e,\sigma} = e^\dagger_\sigma e_\sigma$, $n_{h,\sigma} = h^\dagger_\sigma h_\sigma$ and the abbreviations

$$n_e = \sum_{\sigma=\{\uparrow,\downarrow\}} n_{e,\sigma}, \qquad n_h = \sum_{\sigma=\{\Uparrow,\Downarrow\}} n_{h,\sigma},$$

we can express the Hamiltonian in the occupation number representation as

$$H = \left(\varepsilon_c - \frac{1}{2}V_{c,c}\right)n_e - \left(\varepsilon_v + \frac{1}{2}V_{v,v}\right)n_h + \frac{1}{2}V_{c,c}n_e^2 + \frac{1}{2}V_{v,v}n_h^2 - V_{c,v}n_e n_h. \tag{25}$$

By diagonalization, we obtain the spectral representation of H in terms of multi-particle states

$$H = \sum_k \varepsilon_k \big|k\big\rangle\big\langle k\big|,$$

where $k = (n_{e,\uparrow}, n_{e,\downarrow}, n_{h,\Uparrow}, n_{h,\Downarrow})$ is a multi-index labeling the 16 different electronic configurations which are illustrated in Fig. 4(a, b). If excited states are included and full configuration interaction is taken into account, the diagonalization of H is in general a non-trivial task. In this case, an approximative representation of the Coulomb interaction in terms of number operators as in Eq. (25) can be obtained by the Hartree-Fock approximation [71].

4.1.2 Dissipators

We describe the spontaneous emission and the capture and escape of carriers by dissipators of the type (9). A jump operator A_α describes the transition between two multi-particle states $|i\rangle$ and $|f\rangle$ and is given by the projector $|f\rangle\langle i|$. These transitions are indicated by arrows in Fig. 4(a), e.g. the dissipator connected with $A_\alpha = |X_1\rangle\left\langle e^\uparrow\right|$ describes the capture of a hole into a QD occupied by a single electron leading to the formation of the bright exciton $|X_1\rangle$. By using adjacency matrices to encode the allowed transitions shown in Fig. 4(a), the dissipators for all processes can be written in a compact form as

$$\mathcal{D}_e(\rho) = \sum_{i,f}\mathcal{A}^e_{i,f}\gamma^e_{i\to f}\left(L_{|f\rangle\langle i|}(\rho) + e^{-\beta\Delta\varepsilon^e_{i,f}}L_{|i\rangle\langle f|}(\rho)\right), \tag{26a}$$

$$\mathcal{D}_h(\rho) = \sum_{i,f}\mathcal{A}^h_{i,f}\gamma^h_{i\to f}\left(L_{|f\rangle\langle i|}(\rho) + e^{-\beta\Delta\varepsilon^h_{i,f}}L_{|i\rangle\langle f|}(\rho)\right), \tag{26b}$$

$$\mathcal{D}_0(\rho) = \sum_{i,f}\mathcal{A}^0_{i,f}\gamma^0_{i\to f}\left(L_{|f\rangle\langle i|}(\rho) + e^{-\beta\Delta\varepsilon^0_{i,f}}L_{|i\rangle\langle f|}(\rho)\right), \tag{26c}$$

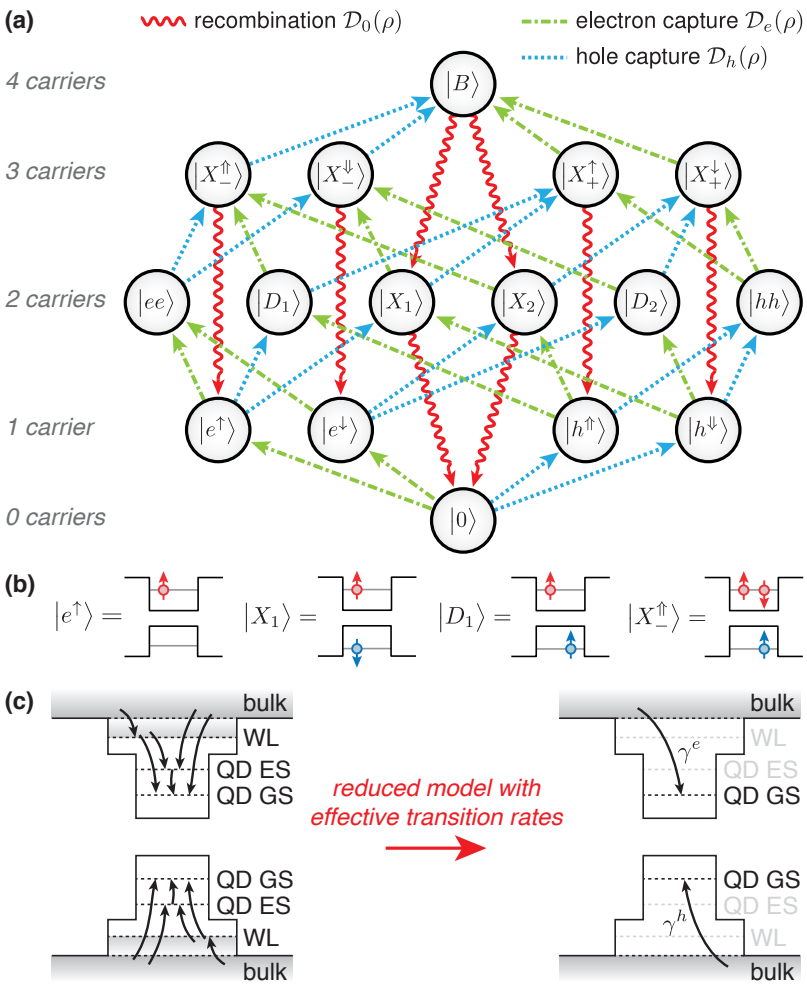

Figure 4: (a) Diagram of electronic states of the QD-Hamiltonian (25) and possible (irreversible) transitions. The arrows indicate capture and recombination, for the corresponding reverse processes (escape, generation) the arrows need to be reversed. We use short notations for the multi-particle states $|n_{e,\uparrow}, n_{e,\downarrow}, n_{h,\Uparrow}, n_{h,\Downarrow}\rangle$: empty QD $|0\rangle = |0,0,0,0\rangle$, single-electron states $|e^{\uparrow}\rangle = |1,0,0,0\rangle$, $e^{\downarrow}\rangle = |0,1,0,0\rangle$, single-hole states $|h^{\Uparrow}\rangle = |0,0,1,0\rangle$, $|h^{\Downarrow}\rangle = |0,0,0,1\rangle$, two-electron state $|ee\rangle = |1,1,0,0\rangle$, two-hole state $|hh\rangle = |0,0,1,1\rangle$, bright excitons $|X_1\rangle = |1,0,0,1\rangle$, $|X_2\rangle = |0,1,1,0\rangle$, dark excitons $|D_1\rangle = |1,0,1,0\rangle$, $|D_2\rangle = |0,1,0,1\rangle$, negative trions $|X_-^{\Uparrow}\rangle = |1,1,1,0\rangle$, $|X_-^{\Downarrow}\rangle = |1,1,0,1\rangle$, positive trions $|X_+^{\uparrow}\rangle = |1,0,1,1\rangle$, $|X_+^{\downarrow}\rangle = |0,1,1,1\rangle$ and the biexciton state $|B\rangle = |1,1,1,1\rangle$. (b) Schematic representation of the QD occupation for some example states. (c) Illustration of the effective scattering cascade in the reduced model involving only the single-particle ground states.

where the *Lindblad superoperator* reads

$$L_A(\rho) = A\rho A^\dagger + \frac{1}{2}\{A^\dagger A, \rho\}$$

and the indices i and f run over all multi-particle states. In accordance with Eq. (23), the effective transition energies are given as

$$\begin{aligned}
\Delta\varepsilon^e_{i,f} &= \varepsilon_i - \varepsilon_f - q\langle\psi\rangle_w - \langle\mu_c\rangle_w\,,\\
\Delta\varepsilon^h_{i,f} &= \varepsilon_i - \varepsilon_f + q\langle\psi\rangle_w + \langle\mu_v\rangle_w\,,\\
\Delta\varepsilon^0_{i,f} &= \varepsilon_i - \varepsilon_f
\end{aligned}$$

and the adjacency matrix elements encoding Pauli blocking and the optical selection rules (conservation of total angular momentum) read

$$\begin{aligned}
\mathcal{A}^e_{i,f} &= \delta_{\langle i|n_e|i\rangle+1,\langle f|n_e|f\rangle} \prod_{\sigma=\{\Uparrow,\Downarrow\}} \delta_{\langle i|n_{h,\sigma}|i\rangle,\langle f|n_{h,\sigma}|f\rangle},\\
\mathcal{A}^h_{i,f} &= \delta_{\langle i|n_h|i\rangle+1,\langle f|n_h|f\rangle} \prod_{\sigma=\{\uparrow,\downarrow\}} \delta_{\langle i|n_{e,\sigma}|i\rangle,\langle f|n_{e,\sigma}|f\rangle},\\
\mathcal{A}^0_{i,f} &= \delta_{\langle i|n_{e,\uparrow}|i\rangle,\langle f|n_{e,\uparrow}|f\rangle}\delta_{\langle i|n_{e,\downarrow}|i\rangle-1,\langle f|n_{e,\downarrow}|f\rangle}\delta_{\langle i|n_{h,\Uparrow}|i\rangle-1,\langle f|n_{h,\Uparrow}|f\rangle}\delta_{\langle i|n_{h,\Downarrow}|i\rangle,\langle f|n_{h,\Downarrow}|f\rangle}+\\
&\quad+\delta_{\langle i|n_{e,\uparrow}|i\rangle-1,\langle f|n_{e,\uparrow}|f\rangle}\delta_{\langle i|n_{e,\downarrow}|i\rangle,\langle f|n_{e,\downarrow}|f\rangle}\delta_{\langle i|n_{h,\Uparrow}|i\rangle,\langle f|n_{h,\Uparrow}|f\rangle}\delta_{\langle i|n_{h,\Downarrow}|i\rangle-1,\langle f|n_{h,\Downarrow}|f\rangle}.
\end{aligned}$$

Finally, we need to specify the transition rates $\gamma_{i\to f}$ occurring in the dissipators Eq. (26).

4.1.3 Transition rate models

The spontaneous decay rates of the various (bright) electronic states of the quantum system can be modeled by the Weisskopf-Wigner rate [72]

$$\gamma^0_{i\to f} = \frac{P_{i,f} d^2_{c,v} n_r}{6\pi\hbar\varepsilon_0 c_0^3} \left(\frac{\varepsilon_i - \varepsilon_f}{\hbar}\right)^3 \left(1 + n_{\mathsf{pt}}\left(\frac{\varepsilon_i - \varepsilon_f}{\hbar}\right)\right), \tag{27}$$

where $n_{\mathsf{pt}}(\omega) = \left(e^{\beta\hbar\omega} - 1\right)^{-1}$ is the thermally induced photon number, n_r is the refractive index of the material, $d_{c,v}$ denotes the interband dipole moment and c_0 is the vacuum speed of light. Due to cavity effects, the decay rate is slightly modified with respect to the free space situation, which is accounted for by the Purcell factors $P_{i,f}$. The Weisskopf-Wigner rate is applicable in low Q optical resonators, where the photonic density of states varies insignificantly over the linewidth of the emitter [17, 73]. Using the parameters given in Appendix F, all decay rates are found to be approximately $10^9\,\mathsf{s}^{-1}$.

For semiconductor QDs, Auger scattering and the Fröhlich coupling typically constitute the dominant capture processes. As a rule of thumb, in the regime of low reservoir carrier densities, the LO-phonon assisted Fröhlich coupling provides the dominant scattering channel, whereas at elevated reservoir carrier densities the Auger scattering becomes increasingly efficient [10, 56, 74]. Due to the relatively large Coulomb matrix elements in semiconductor QDs, the scattering rates into charged states differ significantly from those into neutral states. This effect is known as *Coulomb suppression* or *Coulomb enhancement*, respectively [74].

The scattering rates can be calculated microscopically by Fermi's Golden rule [53–58], however here we restrict ourselves to phenomenological laws for the effective capture rate of continuum carriers into the QD. This effective capture rate approximates the entire scattering cascade, see Fig. 4(c). We model the effective electron capture rates entering Eq. (26a) as

$$\begin{aligned}
\gamma^e_{i\to f}\left(\langle\mu_c\rangle_w, \langle\mu_v\rangle_w, \langle\psi\rangle_w\right) = \frac{1+n_{\mathsf{LO}}}{\tau^e_{\mathsf{LO}}} \frac{1}{e^{\beta\left(E_c - q\langle\psi\rangle_w - \langle\mu_c\rangle_w + a^e_{\mathsf{LO}} + C^e_{i,f}\right)} + 1} +\\
+ \frac{1}{\tau^{e,e}_{\mathsf{Au}}} \frac{\bar{n}_w^2}{1+\bar{n}_w^{2-\gamma^{e,e}_{\mathsf{Au}}}} + \frac{1}{\tau^{e,h}_{\mathsf{Au}}} \frac{\bar{n}_w\bar{p}_w}{1+\left(\bar{n}_w\bar{p}_w\right)^{1-\gamma^{e,h}_{\mathsf{Au}}/2}},
\end{aligned} \tag{28a}$$

and the effective hole capture rates in Eq. (26b) as

$$\gamma^h_{i\to f}\left(\langle\mu_c\rangle_w,\langle\mu_v\rangle_w,\langle\psi\rangle_w\right)=\frac{1+n_{\mathsf{LO}}}{\tau^h_{\mathsf{LO}}}\frac{1}{e^{-\beta\left(E_v-q\langle\psi\rangle_w-\langle\mu_v\rangle-a^h_{\mathsf{LO}}-C^h_{i,f}\right)}+1}+\\+\frac{1}{\tau^{h,h}_{\mathsf{Au}}}\frac{\bar{p}_w^2}{1+\bar{p}_w^{2-\gamma^{h,h}_{\mathsf{Au}}}}+\frac{1}{\tau^{h,e}_{\mathsf{Au}}}\frac{\bar{n}_w\bar{p}_w}{1+\left(\bar{n}_w\bar{p}_w\right)^{1-\gamma^{h,e}_{\mathsf{Au}}/2}}. \tag{28b}$$

with $\bar{n}_w = n_w/n^{\mathsf{crit}}_{\mathsf{Au}}$ and $\bar{p}_w = p_w/p^{\mathsf{crit}}_{\mathsf{Au}}$. Please note that the ambient continuum carrier densities $n_w = N_c F_{1/2}\left(\beta\left(\langle\mu_c\rangle_w - E_c + q\langle\psi\rangle_w\right)\right)$ and $p_w = N_v F_{1/2}\left(\beta\left(E_v - q\langle\psi\rangle_w - \langle\mu_v\rangle_w\right)\right)$ are functions of the averaged macroscopic potentials. The first terms in Eq. (28a) and (28b) describe the LO-phonon assisted relaxation of continuum carriers and the last lines are each attributed to Auger scattering. The number of thermally excited LO-phonons is given by $n_{\mathsf{LO}} = \left(e^{\beta\hbar\omega_{\mathsf{LO}}}-1\right)^{-1}$. The time constants $\tau^\lambda_{\mathsf{LO}}$ as well as the parameters $a^\lambda_{\mathsf{LO}}, \gamma^\lambda_{\mathsf{LO}}$, $\lambda\in\{e,h\}$ are considered as fitting factors that can be extracted from microscopic calculations or experimental data. The phonon assisted capture rates involve the Coulomb enhancement/ suppression factors

$$C^e_{i,f} = \varepsilon_f - \varepsilon_i - \varepsilon_c,$$
$$C^h_{i,f} = \varepsilon_f - \varepsilon_i + \varepsilon_v,$$

which describe the additional attractive or repulsive Coulomb shifts and thereby either enhance (if $C^\lambda_{i,f}<0$, $\lambda\in\{e,h\}$) or decrease (if $C^\lambda_{i,f}>0$, $\lambda\in\{e,h\}$) the capture rate. At low temperatures the effect of Coulomb enhancement or suppression becomes increasingly important. For the Auger-like capture processes the modifications of the capture rates due to Coulomb shifts are assumed to be negligible due to strong screening effects at high carrier densities. The expressions in Eq. (28a) and (28b) take saturation effects at high reservoir carrier densities into account. The functional form is motivated from microscopically computed results presented in Refs. [58, 74]. In the low density limit (Maxwell–Boltzmann approximation) the capture rate models asymptotically take the form

$$\gamma^e_{i\to f}\approx\frac{\left(n_{\mathsf{LO}}+1\right)e^{-\beta a^e_{\mathsf{LO}}}}{\tau^e_{\mathsf{LO}}N_c}e^{-\beta C^e_{i,f}}n_w^{\mathsf{MB}}+\frac{\left(\bar{n}_w^{\mathsf{MB}}\right)^2}{\tau^{e,e}_{\mathsf{Au}}}+\frac{\bar{n}_w^{\mathsf{MB}}\bar{p}_w^{\mathsf{MB}}}{\tau^{e,h}_{\mathsf{Au}}},$$
$$\gamma^h_{i\to f}\approx\frac{\left(n_{\mathsf{LO}}+1\right)e^{-\beta a^h_{\mathsf{LO}}}}{\tau^h_{\mathsf{LO}}N_v}e^{-\beta C^h_{i,f}}p_w^{\mathsf{MB}}+\frac{\left(\bar{p}_w^{\mathsf{MB}}\right)^2}{\tau^{h,h}_{\mathsf{Au}}}+\frac{\bar{n}_w^{\mathsf{MB}}\bar{p}_w^{\mathsf{MB}}}{\tau^{h,e}_{\mathsf{Au}}},$$

showing a linear dependency on the continuum carrier density in the case of LO-phonon assisted capture and a quadratic dependency for the Auger capture processes. Moreover, the Coulomb enhancement and suppression effect becomes apparent in this form. The expression for n_w^{MB} is obtained by replacing $F_{1/2}(\cdot)\to\exp(\cdot)$ in the above definition of n_w (analogous for p_w^{MB}). The parameters $n^{\mathsf{crit}}_{\mathsf{Au}}, p^{\mathsf{crit}}_{\mathsf{Au}}$ and $\gamma^{\lambda,\lambda'}_{\mathsf{Au}}$ $\lambda,\lambda'\in\{e,h\}$ are fitting factors.

4.2 Numerical simulation method

The van Roosbroeck system (1)–(3) is discretized using a Voronoï box based finite volumes method [28, 75] along with a modified Scharfetter-Gummel scheme [76–78] for the discretization of the current densities. The latter one properly reflects the strong degeneration effects of the electron-hole plasma at cryogenic temperatures and takes the Fermi–Dirac statistics and nonlinear diffusion via a generalized Einstein relation fully into account [79]. For time-dependent simulations, an implicit Euler backward discretization along with an adaptive time stepping method is used.

The discretized van Roosbroeck system is solved along with the QME (4) by a full Newton iteration using the electrostatic potential ψ, the quasi-Fermi energies μ_c, μ_v and the density matrix elements $\langle k|\rho|l\rangle$ as independent variables. Therefore, in order to obtain a system of ordinary differential equations, the QME is projected on the Hilbert space basis spanned by the multi-particle eigenstates of H (see Appendix E).

The coupling terms Q stated in Eq. (13) and $S_{n/p}$ given by Eq. (14) introduce a non-local coupling of the van Roosbroeck system with the QME by the spatial profile function w. This has an impact on the sparsity pattern of the Jacobian of the discretized system, since the quantum system interacts in general with a large number of control volumes in its environment. Since the discretized spatial profile function $w_K = |\Omega_K|^{-1} \int_{\Omega_K} \mathrm{d}^3 r\, w(\mathbf{r})$ (with $|\Omega_K|$ being the volume of the K-th Voronoï cell), quickly decays, we discard small matrix elements below a chosen threshold. This preserves the quadratic convergence of the Newton iteration while the overall numerical effort is reduced.

Single-photon sources are typically operated at cryogenic temperatures, which causes serious convergence issues during the numerical solution of the van Roosbroeck system because of the strong depletion of minority carrier densities [80, 81]. By using the temperature embedding method described in Ref. [79], the problem becomes tractable in the vicinity of flat band conditions.

4.3 Device specification

In the numerical simulations presented in the following, we consider the cylindrical GaAs-based p-i-n structure depicted in Fig. 3, where a single QD is placed on the symmetry axis within the center of the intrinsic zone. The total height of the device is 800 nm, the intrinsic layer has a thickness of 200 nm and the doped layers both are 300 nm in height. The doping concentrations are $C = N_D = 2\times10^{18}\,\mathrm{cm}^{-3}$ and $C = -N_A = -10^{19}\,\mathrm{cm}^{-3}$ in the n- and p-domain, respectively. The top radius of the mesa is 0.5 µm and the total radius (at the bottom) is 2.5 µm. The bottom facet is assumed to consist of a highly reflective metal such that it simultaneously acts as an electric contact and a mirror leading to a directed emission in vertical direction. The ohmic contact on the top facet is assumed to consist of an optically transparent material, such that the structure forms a leaky cavity with a low Q factor. The remaining facets are modeled by homogeneous Neumann boundary conditions. The wetting layer (WL) indicated in Fig. 3 is neglected in the simulation. The device is assumed to operate under cryogenic conditions at $T = 50\,\mathrm{K}$.

The numerical simulation exploits the rotational symmetry of the device, such that the computational domain reduces to a 2D cross section with adapted cell volumes.

4.4 Stationary operation

The device operates as a p–i–n diode, which can be seen from the current-voltage curve shown in Fig. 5(c). At cryogenic temperatures the Fermi energy levels in the doped domains are very close to the band edges and therefore the diode's threshold voltage approximately equals the energy band gap of the material (around 1.52 V). The population of the QD states $\langle k\rangle = \langle k|\rho|k\rangle$ can be controlled by the externally applied bias as shown in Fig. 5(a). Since the QD is located within the intrinsic zone of the device, it is most probably unoccupied in the low bias regime. When the applied bias approaches the diode's threshold voltage, the QD population turns into a non-equilibrium distribution: At first, due to the increased continuum carrier densities in the vicinity of the QD, the single-particle and excitonic states are populated. In particular, due to the lack of an radiative decay channel, the dark

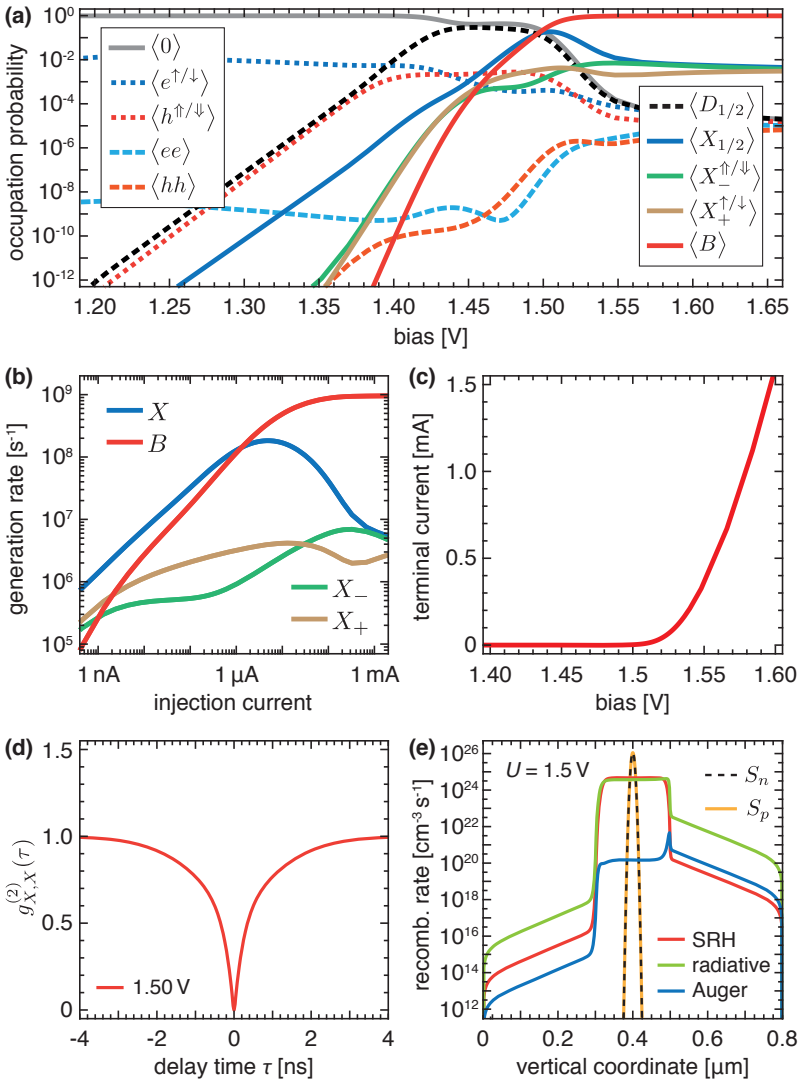

Figure 5: Numerical results at stationary injection. (a) Occupation of the QD states vs. applied bias. (b) Single-photon generation rates of the different emission lines vs. injection current. (c) Current-voltage curve of the diode. (d) Second order correlation function of the photons generated on the exciton line. (e) Comparison of recombination and capture rates of free carriers along the symmetry axis of the device. For the notion of QD states we refer to the caption of Fig. 4.

excitons $\langle D_{1/2} \rangle$ have a high occupation probability. Finally, beyond the threshold, the QD is quickly driven into saturation and the population is dominated by the biexciton state $\langle B \rangle$. Due to Coulomb enhancement and suppression, the population of neutral states is favored in the whole bias range. In particular, Fig. 5(a) shows that the population of the doubly charged states $\langle ee \rangle$ and $\langle hh \rangle$ is strongly suppressed.

The single-photon generation rates of the different emission lines are given by

$$\Gamma_k = \sum_l \mathcal{A}^0_{k,l} \gamma^0_{|k\rangle \to |l\rangle} \langle k \rangle \,. \tag{29}$$

Since the decay rates for all radiative processes are approximately equal, the occupation probabilities are directly proportional to the single-photon generation rates, which are depicted in Fig. 5(b). At low injection currents, the emission spectrum is dominated by photons generated via the decay of bright excitons. Close to the threshold voltage the bright exciton line reaches a maximum and then decreases

while the intensity of the biexciton line grows until it finally saturates. In this regime, the capture rates exceed the radiative decay rates by several orders of magnitude. This simulation result agrees with experimental observations presented in Ref. [65].

Another important figure of merit for single-photon emitters is the second order intensity correlation function of the generated photons

$$g^{(2)}(\tau) = \frac{\left\langle a^\dagger(0)\, a^\dagger(\tau)\, a(\tau)\, a(0)\right\rangle}{\left\langle a^\dagger(0)\, a(0)\right\rangle^2}, \tag{30}$$

where $a^\dagger$ (a) correspond to the creation (annihilation) of a photon and τ is a time delay. A value of $g^{(2)}(0) < 0.5$ indicates the presence of a single-photon Fock state in the radiation field. In our model the decay of an optically active QD state is equivalent to the generation of a corresponding photon. Therefore, the electronic operators can be used to evaluate Eq. (30), cf. Ref. [73]. For the bright exciton line, we identify the photon creation operator with the projector $a^\dagger = |0\rangle\langle X_i|$ (with $i = 1$ or 2) and use the quantum regression theorem [35, 82] to evaluate Eq. (30). The result is presented in Fig. 5(d) and recovers the characteristic dip around $\tau = 0$ for high-quality single-photon sources [15, 65]. Since the present model assumes an ideal quantum emitter and an instantaneous extraction of the generated photons from the cavity, the value of $g^{(2)}(0)$ is exactly zero. For a refined description at this stage, a coherent light-matter interaction must be included in the Hamiltonian and $\mathcal{D}_0(\rho)$ has to be extended by a photon outcoupling mechanism.

Finally, in Fig. 5(e) we show the recombination rate R of the continuum carriers and the capture rates $S_{n/p}$ along the vertical (symmetry) axis of the device. Close to the threshold voltage, the transition of carriers into the QD imposes the dominant loss mechanism of continuum carriers in the vicinity of the QD.

4.5 Pulsed operation

For many applications, the generation of single photons at certain instances of time is required. Electrically driven QD-based single-photon sources offer an easy off-resonant excitation scheme [83], where the QD is excited by short voltage pulses. This process shall be simulated in the following, where we apply rectangular voltage pulses with a fixed duration of 100 ps superimposed on a DC bias of 1.35 V as illustrated in Fig. 6(a). We investigate the impact of the pulse repetition time and the peak bias, which are the key external control parameters. The results of a numerical carrier transport simulation for a single pulse with a peak voltage of 1.6 V are shown in Fig. 6(b, c). Due to the high carrier mobilities at low temperatures (cf. Appendix F), the carriers quickly spread out within the device such that the intrinsic zone is highly populated at the end of the excitation pulse (100 ps). Subsequently, when the applied voltage is switched back to the resting DC bias, the carriers are quickly withdrawn from the intrinsic zone. In the snapshots taken at 116 ps and 200 ps we observe that in particular the vicinity of the QD (which is located on the center of the symmetry axis at 0.4 µm, cf. Fig. 3) is depleted first. Moreover, a conducting channel underneath the insulating region is formed. The plot at 10 ns shows the stationary state reached after a long time.

The impact of the voltage pulse on the occupation of the QD is shown in Fig. 7(a). In the case of an excitation with a peak voltage of 1.6 V (high injection), one first observes a fast occupation of the biexciton state which subsequently decays radiatively. Via the so-called *biexciton-cascade*, the bright exciton states are populated in the following. Comparing the time scales of the carrier transport with the life times of the bright QD states, see Fig. 6(b, c) and Fig. 7(a), it is apparent that the decay of the bright exciton happens a long time after the continuum carriers have left the vicinity of the QD. This

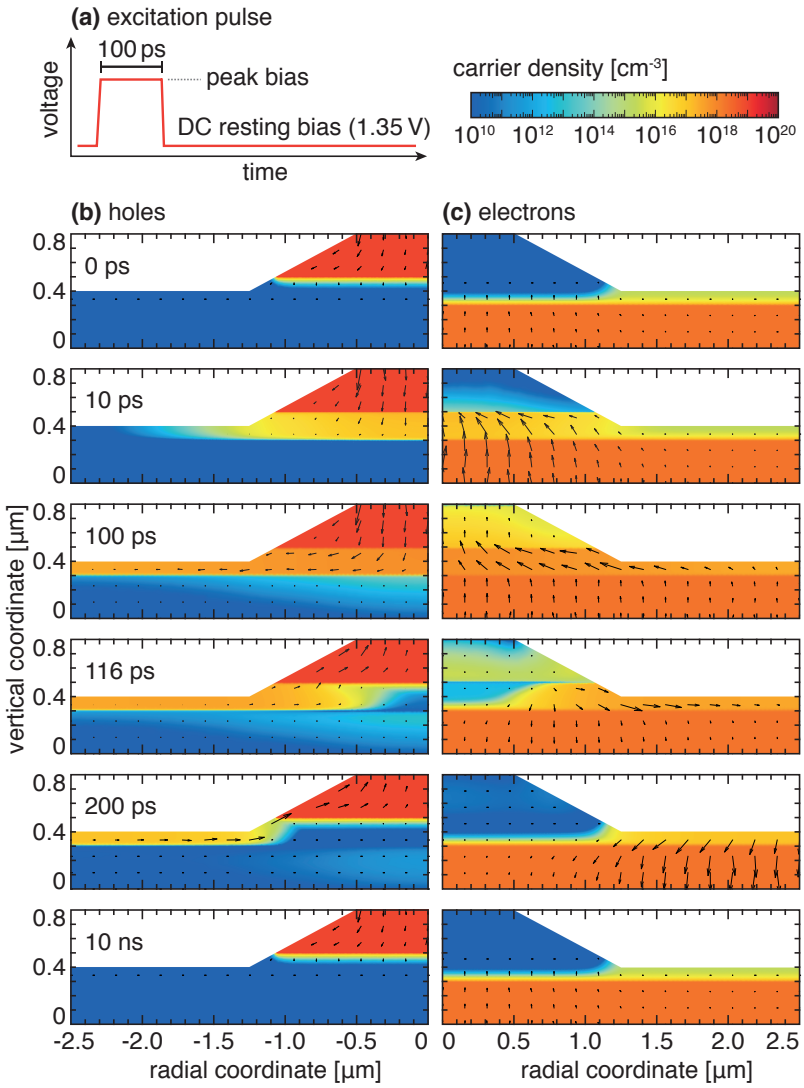

Figure 6: Carrier transport at pulsed excitation. (a) Illustration of the voltage ramp used in the simulations. (b, c) Snapshots of the carrier density distribution on a 2D cross-section at several instances of time. The carrier density is color-coded, the arrows indicate the current density vector field (arrows point into the direction of particle motion). The peak voltage in the simulation was set to 1.6 V.

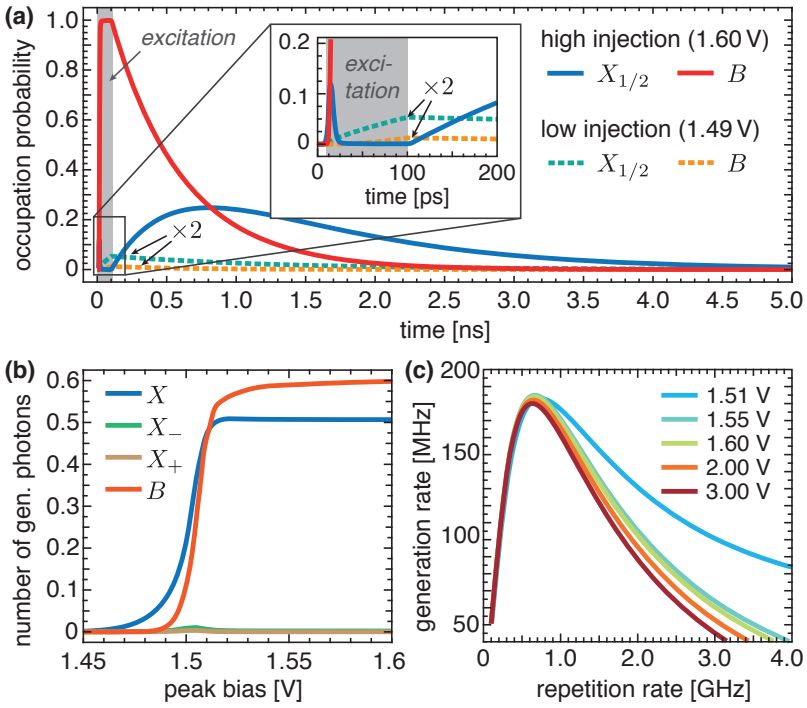

Figure 7: QD occupation and single-photon generation under pulsed excitation. (a) Comparison of the transient exciton and biexciton occupation probabilities in the low and high injection case. In the low injection case the occupation probabilities have been multiplied by a factor 2 for better visibility. (b) Number of generated photons per pulse on the different emission lines for different values of the peak bias. (c) Single-photon generation rate on the bright exciton line vs. repetition frequency of the time-periodic excitation pulse (for different values of the peak bias).

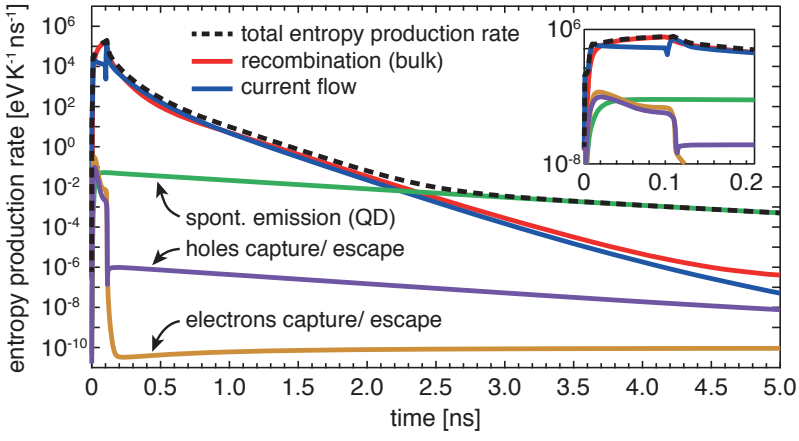

Figure 8: Entropy production rate during the pulse with peak bias 1.6 V. The plot shows the five contributions arising from the individual lines in Eq. (24) and the total entropy production rate as a dashed black line. The inset is a zoom on the first 200 ps.

separation of time scales is of particular importance for the generation of indistinguishable photons [84], since fluctuations of the carrier density in the vicinity of the emitter might shift the generated photon's energy.

Next, we study the impact of the peak bias value. Figure 7(b) shows the number of generated photons for different peak voltages after 10 ns. The number of generated photons on line k until time t is obtained from

$$N_k(t) = \int_0^t \mathrm{d}t' \, \Gamma_k(t') \,,$$

using the single-photon generation rate defined in Eq. (29). The plot clearly reveals the existence of two regimes: A subthreshold (low injection) regime, where the peak voltage is insufficient for the excitation of the QD (cf. Fig. 7(a)), and a high injection regime where the biexciton-cascade can be observed practically after each pulse. For the exciton-photons, this implies a generation efficiency of around 50 % for both polarizations. The generation efficiency of the two differently polarized photons on the biexciton-line is a little higher than 50 %, due to additional recombination during the excitation period, see Fig. 7(a, b).

Finally, we investigate the optimal repetition frequency of the excitation cycle for the generation of single exciton-photons. The optimal repetition frequency $f^* = 1/t^*$ maximizes the number of generated photons per time:

$$\bar{\Gamma}_X(t^*) = \frac{N_X(t^*)}{t^*} = \frac{1}{t^*} \int_0^{t^*} \mathrm{d}t' \, \Gamma_X(t') \to \max \,.$$

Figure 7(c) shows a clear maximum at a pulse repetition rate of $f^* \approx 650\,\mathrm{MHz}$ ($t^* \approx 1.5\,\mathrm{ns}$), which corresponds to a maximum single-photon generation rate of $\bar{\Gamma}_X(t^*) \approx 185\,\mathrm{MHz}$. Even though in this optimal case the photon generation efficiency per pulse shrinks to 28%, the high repetition frequency leads to an enhanced overall performance. Moreover, Fig. 7(c) indicates that this result is practically independent of the peak voltage. In order to obtain the photon emission rate, the generation rate must be multiplied with the photon extraction efficiency [85].

We conclude this section with a consideration of the entropy production during an excitation cycle, which is depicted in Fig. 8. The plot shows, that during the first 2 ns the entropy production rate is clearly governed by the contributions arising from the macroscopic system, whereas at later times the slow decay of the QD-exciton becomes dominant. Our numerical result is in accordance with the theory presented in Sec. 3.4, which predicts a positive entropy production rate at all times.

5 Discussion and outlook

The presented quantum-classical modeling approach can be extended into several directions, mostly by improving some of the simplifying assumptions made above.

First, the inclusion of nanostructures leads to a modification of the local density of electronic states, which has been neglected here. For a more realistic simulation, this effect can be accounted for by a modification of the Fermi–Dirac integral in the vicinity of the nanostructures. Moreover, we introduced the spatial profile function w in order to embed the QD into the spatially resolved macroscopic system. This approximation can be greatly enhanced by incorporating a Schrödinger–Poisson model into the hybrid model system. Besides a better description of the localized charges due to the usage of realistic wave functions, this would also enable a precise modeling of the quantum confined Stark effect and tunnel injection. Previous works on the 1D drift-diffusion-Schrödinger-Poisson system [86, 87] indicate the feasibility of this approach.

Furthermore, semiconductor QDs are often grown in the Stranski–Krastanov mode and therefore come along with a thin WL [1], which has been neglected in the current presentation. The WL represents a 2D-like carrier reservoir, which may be important for a refined description of the carrier scattering cascade from the continuum states to the QDs. For the inclusion of the WL into the drift-diffusion equations, previously developed approaches for quantum wells can be adopted [36, 37].

In this paper, the van Roosbroeck system was used to describe the semi-classical carrier transport on macroscopic scales. For certain applications (e.g. strong internal fields, very short length scales, hot carrier effects) the drift-diffusion approximation becomes insufficient. Higher order models like the *hydrodynamic transport model* or the *six-moment model* are more suitable then [88–90]. In this case, the inclusion of the QD system into the macroscopic model can be achieved in principle along the same lines as in Sec. 2 and 3 of this paper.

In the transient numerical simulations presented in Sec. 4, the system shows an extremely fast response to the external excitation. This behavior can be assigned to the lack of external circuit elements like external resistors and capacitors. If RC elements were included in the simulation, we would expect a slower response of the system to the applied voltage pulses.

Finally, the inclusion of a reversible light-matter interaction into the Hamiltonian of the quantum system enables the simulation of devices showing pronounced cavity-QED effects. In particular, this allows for a spatially resolved simulation of electrically driven nano-VCSELs and exciton-polariton lasers with one or a few QDs as gain material. The self-consistent photon number equation, which is needed for the simulation of laser devices [36, 41], is automatically delivered by the QME. Moreover, the model should also be supplemented with a Helmholtz equation for the calculation of the cavity modes and photon lifetimes. Finally, in the case of multiple QDs a spatially resolved simlation of superradiant emitters [91] may be achieved.

6 Summary

Nowadays, quantum optical technologies are on their way from the lab to real world applications. To advance this development, device engineers will need simulation tools, which combine classical device physics with models from cavity quantum electrodynamics. As a step on this route, we have presented a new modeling approach for the simulation of single and few quantum dot devices.

By connecting semi-classical carrier transport theory with a quantum master equation in Lindlad form, our approach has lead to a hybrid quantum-classical system, that allows for a comprehensive description of electrically driven quantum dot devices on multiple scales: It enables the computation of the spatially resolved carrier transport together with the calculation of quantum optical figures of merit (e.g. photon generation rates, higher order correlation functions) in realistic semiconductor structures in a unified way. This has been demonstrated by numerical simulations of an electrical single-photon source based on a single quantum dot. We have presented a thorough theoretical analysis of the approach and showed that it guarantees the conservation of charge and the consistency with the thermodynamic equilibrium. Finally, we have proven that our hybrid quantum-classical system obeys the second law of thermodynamics.

We believe that our approach serves as a blueprint for the simulation of further quantum dot based photonic devices, in particular nanolasers.

A Boundary conditions

We assume a decomposition of the domain boundary

$$\partial\Omega = \left(\bigcup_i \Gamma_i\right) \cup \Gamma_G \cup \partial\Omega_N$$

into several ohmic contacts, a gate contact and artificial boundaries of the device [28]. The boundary conditions on the artificial boundaries are given by the homogeneous Neumann conditions

$$\mathbf{n} \cdot \nabla\psi = 0, \quad \mathbf{n} \cdot \nabla\mu_c = 0, \quad \mathbf{n} \cdot \nabla\mu_v = 0$$

on $\partial\Omega_N$, where $\mathbf{n}$ denotes the outer normal vector. For the ohmic contacts, we assume the Dirichlet boundary conditions

$$\psi = \psi_{\text{eq}} + U_{\text{appl},i}, \quad \mu_c = \mu_i, \quad \mu_v = \mu_i,$$

on Γ_i, where $U_{\text{appl},i}$ represents the applied voltage at the i-th ohmic contact and $\mu_i = \mu_{\text{eq}} - qU_{\text{appl},i}$. The value of the built-in potential ψ_{eq} is obtained from the local charge neutrality condition at the ohmic boundaries and zeros bias conditions ($\mu_i = \mu_{\text{eq}}\ \forall i$) [75]. On the gate contact Γ_G, we impose a boundary condition of third kind for the electrostatic potential

$$\varepsilon\mathbf{n} \cdot \nabla\psi + \frac{\varepsilon_{\text{ox}}}{d_{\text{ox}}}\left(\psi - U_{\text{appl},G}\right) = 0$$

along with “no flux” conditions for the carriers

$$\mathbf{n} \cdot \nabla\mu_c = 0, \quad \mathbf{n} \cdot \nabla\mu_v = 0.$$

Here, ε_{ox} and d_{ox} describe the permittivity and the thickness of the insulating layer between the semiconductor material and the metal electrode.

B Electrostatic field energy

Following [51], we split the electrostatic potential

$$\psi = \psi_{\text{int}} + \psi_{\text{ext}}$$

into an internal field ψ_{int} generated by the internal charge density and an external field ψ_{ext}, which arises from the built-in doping profile and the applied voltages. Consequently, the Poisson problem (1) on Ω is decomposed into

$$\begin{aligned} -\nabla \cdot \varepsilon\nabla\psi_{\text{int}} &= q\rho_{\text{int}}, \\ -\nabla \cdot \varepsilon\nabla\psi_{\text{ext}} &= qC, \end{aligned}$$

such that the internal field $\psi_{\text{int}} = \psi_{\text{int}}\left(\rho_{\text{int}}\right)$ can be written as a functional of the total internal carrier density

$$\rho_{\text{int}} = p - n + Q\left(\rho\right).$$

On the domain boundaries it holds

$$\begin{aligned} \mathbf{n} \cdot \varepsilon\nabla\psi_{\text{int}} &= 0 && \text{on } \partial\Omega_N, \\ \psi_{\text{int}} &= 0 && \text{on } \Gamma_i, \\ \mathbf{n} \cdot \varepsilon\nabla\psi_{\text{int}} + \frac{\varepsilon_{\text{ox}}}{d_{\text{ox}}}\psi_{\text{int}} &= 0 && \text{on } \Gamma_G, \end{aligned}$$

and

$$\begin{aligned} \mathbf{n}\cdot\varepsilon\nabla\psi_{\text{ext}} &= 0 && \text{on } \partial\Omega_N,\\ \psi_{\text{ext}} &= \psi_{\text{eq}} + U_{\text{appl},i} && \text{on } \Gamma_i,\\ \mathbf{n}\cdot\varepsilon\nabla\psi_{\text{ext}} + \frac{\varepsilon_{\text{ox}}}{d_{\text{ox}}}\psi_{\text{ext}} &= \frac{\varepsilon_{\text{ox}}}{d_{\text{ox}}}U_{\text{appl},G} && \text{on } \Gamma_G. \end{aligned}$$

A variation of the internal carrier density $\rho_{\text{int}} \to \rho_{\text{int}} + a\delta\rho$ ($0 < a \ll 1$ is a small parameter) in the interior of the domain yields a variation of the electrostatic field $\delta\psi$ according to

$$-\nabla\cdot\varepsilon\nabla\delta\psi = q\delta\rho \quad \text{on } \Omega$$

with the same boundary conditions for $\delta\psi$ as for ψ_{int} stated above. The variation of the internal energy given by Eq. (20) leads to

$$\begin{aligned} U_\psi\left(\rho_{\text{int}} + a\delta\rho\right) = U_\psi\left(\rho_{\text{int}}\right) + a\int_\Omega \mathrm{d}^3r\,\varepsilon\nabla\psi_{\text{int}}\left(\rho_{\text{int}}\right)\cdot\nabla\delta\psi + aq\int_\Omega \mathrm{d}^3r\,\delta\rho\psi_{\text{ext}} +\\ + a\frac{\varepsilon_{\text{ox}}}{d_{\text{ox}}}\int_{\Gamma_G}\mathrm{d}A\,\psi_{\text{int}}\left(\rho_{\text{int}}\right)\delta\psi + \mathcal{O}\left(a^2\right). \end{aligned}$$

Finally, using the identity

$$\int_\Omega \mathrm{d}^3r\,\varepsilon\nabla\psi_{\text{int}}\left(\rho_{\text{int}}\right)\cdot\nabla\delta\psi = q\int_\Omega \mathrm{d}^3r\,\psi_{\text{int}}\left(\rho_{\text{int}}\right)\delta\rho + \int_{\Gamma_G}\mathrm{d}\mathbf{A}\cdot\nabla\delta\psi\,\varepsilon\psi_{\text{int}}\left(\rho_{\text{int}}\right),$$

one obtains the Gâteaux-derivative

$$\lim_{a\to 0}\frac{U_\psi\left(\rho_{\text{int}} + a\delta\rho\right) - U_\psi\left(\rho_{\text{int}}\right)}{a} = q\int_\Omega \mathrm{d}^3r\,\left(\psi_{\text{int}}\left(\rho_{\text{int}}\right) + \psi_{\text{ext}}\right)\delta\rho.$$

The central feature of the field's internal energy expression Eq. (20) is [50, 51]

$$\frac{\delta U_\psi}{\delta\rho} = q\psi. \tag{31}$$

C Entropy production rate

This section gives some details on the derivation of the expression (24) for the entropy production rate. Starting from Eq. (15), one obtains by using Eq. (17) and (18) the entropy production rate as

$$\begin{aligned} \frac{\mathrm{d}S_{\text{tot}}}{\mathrm{d}t} = &-\frac{1}{T}\int_\Omega \mathrm{d}^3r\,\left(\frac{\partial u_{\text{cl}}\left(n,p\right)}{\partial t} - T\frac{\partial s_{\text{cl}}\left(n,p\right)}{\partial t}\right)\\ &-\frac{1}{T}\left(\mathrm{tr}\left(H\mathcal{L}\left(\rho\right)\right) + k_BT\mathrm{tr}\left(\log\left(\rho\right)\mathcal{L}\left(\rho\right)\right)\right)\\ &-\frac{1}{T}\frac{\mathrm{d}U_\psi}{\mathrm{d}t} + \sum_{i\geq 1}\frac{\mu_i}{qT}\int_{\Gamma_i}\mathrm{d}\mathbf{A}\cdot\left(\mathbf{j}_n + \mathbf{j}_p\right). \end{aligned}$$

Taking the partial time derivatives, using the state equations (5), Eq. (31) and

$$\frac{\mathrm{d}U_\psi}{\mathrm{d}t} = \int_\Omega \mathrm{d}^3r\,q\psi\frac{\partial\left(p - n + Q\left(\rho\right)\right)}{\partial t},$$

we arrive at

$$\begin{aligned}\frac{\mathrm{d}S_{\text{tot}}}{\mathrm{d}t} = &-\frac{1}{T}\int_\Omega \mathrm{d}^3 r\, \left(\mu_c \frac{\partial n}{\partial t} - \mu_v \frac{\partial p}{\partial t}\right) \\ &- \frac{1}{T}\left(\mathrm{tr}\left(H\mathcal{L}\left(\rho\right)\right) + k_B T \mathrm{tr}\left(\log\left(\rho\right)\mathcal{L}\left(\rho\right)\right)\right) \\ &+ \frac{q}{T}\left\langle\psi\right\rangle_w \mathrm{tr}\left(N\mathcal{L}\left(\rho\right)\right) \\ &+ \sum_{i\geq 1}\frac{\mu_i}{qT}\int_{\Gamma_i}\mathrm{d}\mathbf{A}\cdot\left(\mathbf{j}_n + \mathbf{j}_p\right),\end{aligned}$$

where we have explicitly used Eq. (13) for the charge density of the quantum system. For different $Q\left(\rho\right)$ and multiple QDs, the calculation follows the same lines. With the help of the carrier transport equations (2)–(3), the macroscopic capture rates (14), partial integration and the boundary conditions given in Appendix A, this is

$$\begin{aligned}\frac{\mathrm{d}S_{\text{tot}}}{\mathrm{d}t} = &\frac{1}{T}\int_\Omega \mathrm{d}^3 r\, \left(\mu_c - \mu_v\right) R \\ &+ \frac{1}{qT}\int_\Omega \mathrm{d}^3 r\, \left(\mathbf{j}_n\cdot\nabla\mu_c + \mathbf{j}_p\cdot\nabla\mu_v\right) \\ &+ \frac{1}{T}\left\langle\mu_c\right\rangle_w \mathrm{tr}\left(ND_e\right) + \frac{1}{T}\left\langle\mu_v\right\rangle_w \mathrm{tr}\left(ND_h\right) \\ &- \frac{1}{T}\left(\mathrm{tr}\left(H\mathcal{D}\left(\rho\right)\right) + k_B T \mathrm{tr}\left(\log\left(\rho\right)\mathcal{D}\left(\rho\right)\right)\right) \\ &+ \frac{q}{T}\left\langle\psi\right\rangle_w \mathrm{tr}\left(N\mathcal{D}\left(\rho\right)\right).\end{aligned}$$

In the above expression, the surface integrals have canceled out. Using Eq. (11) and (12), one finally arrives at Eq. (24).

D Second law of thermodynamics

In this section we proof the non-negativity of the entropy production rate (24) of the hybrid system (1)–(4).

First, we introduce the (auxiliary) density matrices

$$\rho_0^* = \frac{1}{Z_0^*}e^{-\beta H}, \tag{32a}$$

$$\rho_e^* = \frac{1}{Z_e^*}e^{-\beta\left(H-\mu_c^{\text{eff}}N\right)}, \tag{32b}$$

$$\rho_h^* = \frac{1}{Z_h^*}e^{-\beta\left(H-\mu_v^{\text{eff}}N\right)} \tag{32c}$$

with $\mu_{c/v}^{\text{eff}} = \left\langle\mu_{c/v}\right\rangle_w + q\left\langle\psi\right\rangle_w$. Using Eq. (23) it can be shown by direct calculation that $\mathcal{D}_\nu\left(\rho_\nu^*\right) = 0$, $\nu\in\{0,e,h\}$, for the dissipators given in Eq. (11). Then it holds [92, 93]

$$\mathrm{tr}\left(\left(\log\rho_\nu^* - \log\rho\right)\mathcal{D}_\nu\left(\rho\right)\right) \geq 0 \tag{33}$$

for $\nu\in\{0,e,h\}$.

The entropy production rate Eq. (24) can be written in the form

$$\begin{aligned}\frac{\mathrm{d}S_{\text{tot}}}{\mathrm{d}t} &= k_B \int_\Omega \mathrm{d}^3 r\, \beta\left(\mu_c - \mu_v\right)\left(1 - e^{-\beta(\mu_c-\mu_v)}\right)\sum_j r_j \\ &+ \frac{1}{q^2 T}\int_\Omega \mathrm{d}^3 r\, \left(\sigma_n \left|\nabla\mu_c\right|^2 + \sigma_p \left|\nabla\mu_v\right|^2\right) \\ &+ k_B \mathrm{tr}\left(\left(\log\rho_0^* - \log\rho\right)\mathcal{D}_0\left(\rho\right)\right) \\ &+ k_B \mathrm{tr}\left(\left(\log\rho_e^* - \log\rho\right)\mathcal{D}_e\left(\rho\right)\right) \\ &+ k_B \mathrm{tr}\left(\left(\log\rho_h^* - \log\rho\right)\mathcal{D}\left(\rho\right)\right),\end{aligned} \tag{34}$$

where we have used Eqns. (6), (32), the trace conservation property of the dissipator and a recombination rate of the form [75]

$$R = \left(1 - e^{-\beta(\mu_c-\mu_v)}\right)\sum_j r_j\left(n,p,\psi\right).$$

Here, j labels the recombination channels and the functions $r_j = r_j\left(n,p,\psi\right)$ are assumed to be non-negative. Using the inequalities (33) and $x\left(1-e^{-x}\right) \geq 0\ \forall x \in \mathbb{R}$, it is easy to see that each line of Eq. (34) is non-negative.

E Projection on eigenstates

In order to convert Eq. (4) into a system of ODEs, the density matrix must be projected on a basis of the Hilbert space of the quantum system. In order to reduce the numerical complexity, it is beneficial to choose the eigenbasis of the Hamiltonian H, for which we assume the spectral representation

$$H = \sum_k \varepsilon_k \left|\varphi_k\right\rangle\left\langle\varphi_k\right|.$$

For the sake of simplicity, we consider the energy spectrum $\{\varepsilon_k\}$ to be non-degenerate here. Then, the jump operators are projectors between energy eigenstates $A_\alpha \to A_{i,j} = \left|\varphi_i\right\rangle\left\langle\varphi_j\right|$. The equations of motion for the diagonal elements of the density matrix are obtained as

$$\partial_t\left\langle\varphi_k\right|\rho\left|\varphi_k\right\rangle = \sum_j\left(\mathcal{M}_{k,j}\left\langle\varphi_j\right|\rho\left|\varphi_j\right\rangle - \mathcal{M}_{j,k}\left\langle\varphi_k\right|\rho\left|\varphi_k\right\rangle\right),$$

whereas the off-diagonal elements $k \neq l$ obey

$$\partial_t\left\langle\varphi_k\right|\rho\left|\varphi_l\right\rangle = -\frac{i}{\hbar}\left(\varepsilon_k - \varepsilon_l\right)\left\langle\varphi_k\right|\rho\left|\varphi_l\right\rangle - \frac{1}{2}\sum_j\left(\mathcal{M}_{j,k} + \mathcal{M}_{j,l}\right)\left\langle\varphi_k\right|\rho\left|\varphi_l\right\rangle$$

with the (non-negative) transition rate matrix elements

$$\begin{aligned}\mathcal{M}_{i,j} &= \gamma_{i,j} + \hat{\gamma}_{j,i} \\ &= \gamma_{i,j}\left(1 + e^{-\beta\left(\varepsilon_j - \varepsilon_i - \left(\left\langle\mu_{i,j}\right\rangle_w + q\left\langle\psi\right\rangle_w\right)\ell_{i,j}\right)}\right) \geq 0.\end{aligned}$$

Obviously, in the case of non-degenerate energy spectra the diagonal elements decouple from the off-diagonal elements. The off-diagonal elements are fully decoupled each and show damped oscillations (dephasing).

The above observation has strong implications on the numerical simulations. Starting from the thermal equilibrium state, where only diagonal elements of the density matrix are occupied, the dynamics never excite any off-diagonal elements (in the representation using the eigenbasis of H). Hence, the off-diagonal elements can be omitted from the numerical simulation. This is a consequence of the restriction to dissipators of the form (9), which satisfy the quantum detailed balance condition. This feature is of outstanding importance, since the number of degrees of freedom of the quantum system grows only with N instead of N^2, where N is the dimension of the (possibly truncated) Hilbert space.

F Parameters and auxiliary models

This section lists the parameters used in the numerical simulations presented in Sec. 4.

F.1 Van Roosbroeck system

We use GaAs parameters at $T = 50$ K. The effective masses are $m_e^* = 0.068\, m_0$, $m_h^* = 0.503\, m_0$, where m_0 denotes the (free) electron mass and the band edge energies are taken as $E_v = 0$ eV and $E_c = 1.516$ eV. The (static) relative permittivity is set to $\varepsilon_r = 12.9$, the LO-phonon energy is $\hbar\omega_{\mathsf{LO}} = 36.5$ meV and the refractive index is $n_r = 3.55$ for the considered wavelengths (around 950 nm). The recombination rate in Eqns. (2), (3) is modeled as

$$R = R_{\mathsf{SRH}} + R_{\mathsf{sp}} + R_{\mathsf{Au}}$$

with

$$\begin{aligned} R_{\mathsf{SRH}} &= \frac{np}{\tau_p\,(n + n_d) + \tau_n\,(p + p_d)} \left(1 - e^{-\beta(\mu_c - \mu_v)}\right), \\ R_{\mathsf{sp}} &= Bnp\left(1 - e^{-\beta(\mu_c - \mu_v)}\right), \\ R_{\mathsf{Au}} &= \left(C_{\mathsf{Au}}^n n + C_{\mathsf{Au}}^p p\right) np\left(1 - e^{-\beta(\mu_c - \mu_v)}\right) \end{aligned}$$

and $n_d = ne^{\beta(E_T - q\psi - \mu_c)}$, $p_d = pe^{-\beta(E_T - q\psi - \mu_v)}$. The non-radiative life times are sensitive to the impurity concentration and modeled via $\tau_{n/p} = \tau_{n/p,0}/\left(1 + \left(|C|/C_{\mathsf{ref}}\right)^{\gamma_{\mathsf{SRH}}}\right)$ with $\tau_{n,0} = \tau_{p,0} = 10$ ns, $\gamma_{\mathsf{SRH}} = 1.72$ and $C_{\mathsf{ref}} = 9 \times 10^{17}\,\mathsf{cm}^{-3}$ [94]. The trap energy level E_T is assumed to be in the center of the energy gap. The radiative recombination coefficient is taken as $B = 1.06 \times 10^{-8}\,\mathsf{cm}^{-3}\,\mathsf{s}^{-1}$ and the Auger recombination coefficients are set to $C_{\mathsf{Au}}^n = 6 \times 10^{-30}\,\mathsf{cm}^{-6}\,\mathsf{s}^{-1}$, $C_{\mathsf{Au}}^p = 1.6 \times 10^{-29}\,\mathsf{cm}^{-6}\,\mathsf{s}^{-1}$ [94]. The conductivities are given as $\sigma_n = qM_n n$, $\sigma_p = qM_p p$, where we model the carrier mobilities $M_{n/p}$ according to the model given in Ref. [95]. The mobility model is reported to hold down to $T = 50$ K. The doping densities are set to $C = N_D = 2 \times 10^{18}\,\mathsf{cm}^{-3}$ in the n-domain and $C = -N_A = -1 \times 10^{19}\,\mathsf{cm}^{-3}$ in the p-domain. Despite the low temperatures, we assume complete ionization due to the metal-insulator transition at heavy doping [96].

F.2 Open quantum system

The eigenenergies of the Hamiltonian (25) are obtained from the parabolic/step-like confinement potential (relative to the respective continuum band edge) $U_\lambda(r, z) = -U_0^\lambda \Theta\left(h/2 - |z|\right) + \frac{1}{2} m_\lambda^* \omega_{\lambda,0}^2 r^2$, $\lambda \in \{e, h\}$, by solving the stationary Schrödinger equation at flat band conditions [54, 70]. The parameters for the InGaAs-QD are taken as $U_e = 350$ meV, $U_h = 170$ meV, $m_e^* = 0.067\, m_0$,

$m_h^* = 0.15\, m_0$ [54] and $\hbar\omega_{e,0} = 45.5$ meV, $\hbar\omega_{h,0} = 20.3$ meV. The QD height is assumed as $h = 3$ nm. For the computation of the Coulomb matrix elements we set the background dielectric permittivity to $\varepsilon_r = 12.5$ [54].

With the parameters above, the QD conduction band ground state ε_c is found at 137.7 meV below the continuum band edge and the QD valence band ground state ε_v is 44.7 meV above the valence band edge. The Coulomb matrix elements are obtained as $V_{c,c} = 23.2$ meV, $V_{v,v} = 24.5$ meV and $V_{c,v} = 23.7$ meV. The interband dipole moment is assumed as $d_{c,v} = q \times 0.6$ nm and the Purcell factor is set to $P_{i,f} = 1.8$ for all allowed optical transitions. The emission energies are obtained around 1.31 eV with radiative life times of approximately 1 ns according to Eq. (27). The fitting parameters in the carrier scattering rates are set to $\tau_{\mathsf{LO}}^e = \tau_{\mathsf{LO}}^h = 10$ ps, $a_{\mathsf{LO}}^e = 25$ meV, $a_{\mathsf{LO}}^h = 7$ meV, $\tau_{\mathsf{Au}}^{\lambda,\lambda'} = 1$ ps, $\gamma_{\mathsf{Au}}^{\lambda,\lambda'} = 0.7$ (for all $\lambda, \lambda' \in \{e, h\}$), $n_{\mathsf{Au}}^{\mathsf{crit}} = 1 \times 10^{19}$ cm^{-3} and $p_{\mathsf{Au}}^{\mathsf{crit}} = 5 \times 10^{18}$ cm^{-3}.

References

[1] D. Bimberg, M. Grundmann and N. N. Ledentsov. *Quantum Dot Heterostructures*. John Wiley & Sons (1999).

[2] P. Michler (editor). *Single Quantum Dots*, Vol. 90 of *Topics in Applied Physics*. Springer: Berlin, Heidelberg (2003).

[3] P. Bhattacharya and Z. Mi. Quantum-dot optoelectronic devices. *P. IEEE* **95**(9), 1723–1740 (2007).

[4] P. Michler (editor). *Single Semiconductor Quantum Dots*. NanoScience and Technology. Springer: Berlin, Heidelberg (2009).

[5] J. Wu, S. Chen, A. Seeds and H. Liu. Quantum dot optoelectronic devices: Lasers, photodetectors and solar cells. *J. Phys. D Appl. Phys.* **48**(36), 363001 (2015).

[6] D. Bimberg and U. W. Pohl. Quantum dots: promises and accomplishments. *Materials Today* **14** (9), 388–397 (2011).

[7] S. Noda. Seeking the ultimate nanolaser. *Science* **314**(5797):260–261 (2006).

[8] C. Gies, M. Florian, P. Gartner and F. Jahnke. The single quantum dot-laser: Lasing and strong coupling in the high-excitation regime. *Opt. Express* **19**(15), 14370–14388 (2011).

[9] S. Strauf and F. Jahnke. Single quantum dot nanolaser. *Laser & Photonics Reviews* **5**(5), 607–633, (2011).

[10] W. W. Chow and F. Jahnke. On the physics of semiconductor quantum dots for applications in lasers and quantum optics. *Prog. Quant. Electron.* **37**(3), 109–184 (2013).

[11] C. Schneider, A. Rahimi-Iman, N. Y. Kim, J. Fischer, I. G. Savenko, M. Amthor, M. Lermer, A. Wolf, L. Worschech, V. D Kulakovskii, I. A. Shelykh, M. Kamp, S. Reitzenstein, A. Forchel, Y. Yamamoto and S. Höfling An electrically pumped polariton laser. *Nature* **497**(7449), 348–352 (2013).

[12] T. Akiyama, M. Sugawara and Y. Arakawa. Quantum-dot semiconductor optical amplifiers. *P. IEEE* **95**(9), 1757–1766 (2007).

[13] P. Michler, A. Kiraz, C. Becher, W. V. Schoenfeld, P. M. Petroff, L. Zhang, E. Hu, and A Imamoglu. A quantum dot single-photon turnstile device. *Science* **290**(5500):2282–2285 (2000).

[14] C. Santori, D. Fattal, J. Vučković, G. S. Solomon and Y. Yamamoto. Indistinguishable photons from a single-photon device. *Nature* **419**(6907), 594–597 (2002).

[15] C. Santori, D. Fattal, and Y. Yamamoto. *Single-photon Devices and Applications*. Wiley, Weinheim (2010).

[16] S. Buckley, K. Rivoire and J. Vučković. Engineered quantum dot single-photon sources. *Rep. Prog. Phys.* **75**(12), 126503 (2012).

[17] P. Lodahl, S. Mahmoodian and S. Stobbe. Interfacing single photons and single quantum dots with photonic nanostructures. *Rev. Mod. Phys.* **87**(2), 347–400 (2015).

[18] H. J. Kimble. The quantum internet. *Nature* **453**(7198), 1023–1030 (2008).

[19] N. Gisin, G. Ribordy, W. Tittel and H. Zbinden. Quantum cryptography. *Rev. Mod. Phys.* **74**(1), 145 (2002).

[20] E. Knill, R. Laflamme and G. J. Milburn. A scheme for efficient quantum computation with linear optics. *Nature* **409**(6816), 46–52 (2001).

[21] B. A. Kairdolf, A. M. Smith, T. H. Stokes, M. D. Wang, A. N. Young and S. Nie. Semiconductor quantum dots for bioimaging and biodiagnostic applications. *Annu. Rev. Anal. Chem.* **6**, 143–162 (2013).

[22] C. Gies, M. Florian, F. Jahnke, and P. Gartner. *Modeling single quantum dots in microcavities.* In F. Jahnke (editor): *Quantum Optics with Semiconductor Nanostructures*, Woodhead Publishing Series in Electronic and Optical Materials, Ch. 3, 78–114, Woodhead Publishing (2012).

[23] A. Steinhoff, P. Gartner, M. Florian and F. Jahnke. Treatment of carrier scattering in quantum dots beyond the Boltzmann equation. *Phys. Rev. B* **85**, 205144 (2012).

[24] N. Ishida, T. Byrnes, F. Nori and Y. Yamamoto. Photoluminescence of a microcavity quantum dot system in the quantum strong-coupling regime. *Sci. Rep.* **3**, 1180 (2013).

[25] S. C. Kuhn, A. Knorr, S. Reitzenstein and M. Richter. Cavity assisted emission of single, paired and heralded photons from a single quantum dot device. *Opt. Express* **24**(22), 25446–25461 (2016).

[26] C. Hopfmann, A. Carmele, A. Musiał, C. Schneider, M. Kamp, S. Höfling, A. Knorr and S. Reitzenstein. Transition from Jaynes-Cummings to Autler-Townes ladder in a quantum dot–microcavity system. *Phys. Rev. B* **95**(3), 035302 (2017).

[27] W. van Roosbroeck. Theory of the flow of electrons and holes in germanium and other semiconductors. *Bell Sys. Tech. J.* **29**(4), 560–607 (1950).

[28] S. Selberherr. *Analysis and Simulation of Semiconductor Devices*. Springer: Wien (1984).

[29] A. Martí, L. Cuadra and A. Luque. Quasi-drift diffusion model for the quantum dot intermediate band solar cell. *IEEE T. Electron Dev.* **49**(9), 1632–1639 (2002).

[30] M. Gioannini, A. P. Cedola, N. Di Santo, F. Bertazzi and F. Cappelluti. Simulation of quantum dot solar cells including carrier intersubband dynamics and transport. *IEEE J. Photovolt.* **3**(4), 1271–1278 (2013).

[31] M. Kantner, U. Bandelow, T. Koprucki, J.-H. Schulze, A. Strittmatter and H.-J. Wünsche. Efficient current injection into single quantum dots through oxide-confined p-n-diodes. *IEEE T. Electron Dev.* **63**(5), 2036–2042 (2016).

[32] E. B. Davies. Markovian master equations. *Comm. Math. Phys.* **39**(2), 91–110 (1974).

[33] G. Lindblad. On the generators of quantum dynamical semigroups. *Comm. Math. Phys.* **48**(2), 119–130 (1976).

[34] V. Gorini, A. Kossakowski and E. C. G. Sudarshan. Completely positive dynamical semigroups of n-level systems. *J. Math. Phys.* **17**(5), 821–825 (1976).

[35] H.-P. Breuer and F. Petruccione. *The Theory of Open Quantum Systems*. Oxford University Press (2002).

[36] M. Grupen and K. Hess. Simulation of carrier transport and nonlinearities in quantum-well laser diodes. *IEEE J. Quantum Elect.* **34**(1), 120–140 (1998).

[37] S. Steiger, R. G. Veprek and B. Witzigmann. Unified simulation of transport and luminescence in optoelectronic nanostructures. *J. Comput. Electron.* **7**(4), 509–520 (2008).

[38] T. Koprucki, A. Wilms, A. Knorr and U. Bandelow. Modeling of quantum dot lasers with microscopic treatment of Coulomb effects. *Opt. Quant. Electron.* **42**(11-13), 777–783 (2011).

[39] P. A. Markovich. *The stationary semiconductor device equations*. Springer: Wien (1986).

[40] S. R. de Groot and P. Mazur. *Non-equilibrium Thermodynamics*. Dover Books on Physics (1962).

[41] U. Bandelow, H. Gajewski, and R. Hünlich. *Fabry-Perot lasers: Thermodynamics-based modeling*. In J. Piprek (editor): *Optoelectronic Devices*, Ch. 3, 63–85, Springer (2005).

[42] R. Alicki. On the detailed balance condition for non-hamiltonian systems. *Rep. Math. Phys.* **10** (2), 249–258 (1976).

[43] A. Kossakowski, A. Frigerio, V. Gorini and M. Verri. Quantum detailed balance and KMS condition. *Comm. Math. Phys.* **57**(2), 97–110 (1977).

[44] J. Gemmer, M. Michel and G. Mahler. *Quantum Thermodynamics*, Vol. 657 of *Lecture Notes in Physics*. Springer: Berlin, Heidelberg (2004).

[45] R. Kosloff. Quantum thermodynamics: A dynamical viewpoint. *Entropy* **15**(6), 2100–2128 (2013).

[46] M. Esposito, M. A. Ochoa and M. Galperin. Quantum thermodynamics: A nonequilibrium Green's function approach. *Phys. Rev. Lett.* **114**(8), 080602 (2015).

[47] J. Goold, M. Huber, A. Riera, L. del Rio and P. Skrzypczyk. The role of quantum information in thermodynamics: A topical review. *J. Phys. A Math. Theor.* **49**(14), 143001 (2016).

[48] J. P. Pekola. Towards quantum thermodynamics in electronic circuits. *Nat. Phys.* **11**(2), 118–123 (2015).

[49] P. Strasberg, G. Schaller, T. Brandes and M. Esposito. Quantum and information thermodynamics: A unifying framework based on repeated interactions. *Phys. Rev. X* **7**(2), 021003 (2017).

[50] G. Albinus, H. Gajewski and R. Hünlich. Thermodynamic design of energy models of semiconductor devices. *Nonlinearity* **15**(2), 367–383 (2002).

[51] G. Albinus. Thermodynamics of energy models of semiconductor devices. *J. Appl. Math. Mech. (ICIAM/GAMM 95 Applied Analysis)* **76**, 289–292 (1996).

[52] R. Alicki. The Markov master equations and the Fermi golden rule. *Int. J. Theor. Phys.* **16**(5), 351–355 (1977).

[53] I. Magnúsdóttir, A. V. Uskov, S. Bischoff, B. Tromborg and J. Mørk. One- and two-phonon capture processes in quantum dots. *J. Appl. Phys.* **92**(10), 5982 (2002).

[54] T. R. Nielsen, P. Gartner and F. Jahnke. Many-body theory of carrier capture and relaxation in semiconductor quantum-dot lasers. *Phys. Rev. B* **69**, 235314 (2004).

[55] E. Malic, M. J. P. Bormann, P. Hövel, M. Kuntz, D. Bimberg, A. Knorr and E. Schöll. Coulomb damped relaxation oscillations in semiconductor quantum dot lasers. *IEEE J. Sel. Top. Quant.* **13** (5), 1242–1248 (2007).

[56] M.-R. Dachner, E. Malic, M. Richter, A. Carmele, J. Kabuss, A. Wilms, J.-E. Kim, G. Hartmann, J. Wolters, U. Bandelow and A. Knorr. Theory of carrier and photon dynamics in quantum dot light emitters. *Phys. Status Solidi B* **247**(4), 809–828 (2010).

[57] J. M. Miloszewski, M. S. Wartak, S. G. Wallace and S. Fafard. Theoretical investigation of carrier capture and escape processes in cylindrical quantum dots. *J. Appl. Phys.* **114**(15), 154311 (2013).

[58] A. Wilms, P. Mathé, F. Schulze, T. Koprucki, A. Knorr and U. Bandelow. Influence of the carrier reservoir dimensionality on electron-electron scattering in quantum dot materials. *Phys. Rev. B* **88**, 235421 (2013).

[59] H. Gajewski and K. Gärtner. On the discretization of van Roosbroeck's equations with magnetic field. *J. Appl. Math. Mech.* **76**(5), 247–264 (1996).

[60] L. Onsager. Reciprocal relations in irreversible processes. I. *Phys. Rev.* **37**(4), 405 (1931).

[61] M. Grmela and H. C. Öttinger. Dynamics and thermodynamics of complex fluids. I. Development of a general formalism. *Phys. Rev. E* **56**, 6620–6632 (1997).

[62] H. C. Öttinger. The geometry and thermodynamics of dissipative quantum systems. *Europhys. Lett.* **94**(1), 10006 (2011).

[63] A. Mielke. On thermodynamical couplings of quantum mechanics and macroscopic systems. In P. Exner, W. König, and H. Neidhardt (editors): *Mathematical Results in Quantum Mechanics*, 331–348, World Scientific: Singapore (2015)

[64] M. Mittnenzweig and A. Mielke. An entropic gradient structure for Lindblad equations and couplings of quantum systems to macroscopic models. *J. Stat. Phys.* **167**(2), 205 (2017).

[65] Z. Yuan, B. E. Kardynal, R. M. Stevenson, A. J. Shields, C. J. Lobo, K. Cooper, N. S. Beattie, D. A. Ritchie and M. Pepper. Electrically driven single-photon source. *Science* **295**(5552), 102–105 (2002).

[66] A. J. Bennett, D. C. Unitt, P. See, A. J. Shields, P. Atkinson, K. Cooper and D. A. Ritchie. Electrical control of the uncertainty in the time of single photon emission events. *Phys. Rev. B* **72**(3), 033316 (2005).

[67] M. B. Ward, T. Farrow, P. See, Z. L. Yuan, O. Z. Karimov, A. J. Bennett, A. J. Shields, P. Atkinson, K. Cooper and D. A. Ritchie. Electrically driven telecommunication wavelength single-photon source. *Appl. Phys. Lett.* **90**(6), 063512 (2007).

[68] W. Unrau, D. Quandt, J.-H. Schulze, T. Heindel, T. D. Germann, O. Hitzemann, A. Strittmatter, S. Reitzenstein, U. W. Pohl and D. Bimberg. Electrically driven single-photon source based on a site-controlled quantum dot with self-aligned current injection. *Appl. Phys. Lett.* **101**(21), 211119 (2012).

[69] A. Schlehahn, R. Schmidt, C. Hopfmann, J.-H. Schulze, A. Strittmatter, T. Heindel, L. Gantz, E. R. Schmidgall, D. Gershoni and S. Reitzenstein. Generating single photons at gigahertz modulation-speed using electrically controlled quantum dot microlenses. *Appl. Phys. Lett.* **108** (2), 021104 (2016).

[70] A. Wojs, P. Hawrylak, S. Fafard and L. Jacak. Electronic structure and magneto-optics of self-assembled quantum dots. *Phys. Rev. B* **54**(8), 5604–5608 (1996).

[71] N. Baer, P. Gartner and F. Jahnke. Coulomb effects in semiconductor quantum dots. *Eur. Phys. J. B* **42**(2), 231–237 (2004).

[72] V. Weisskopf and E. Wigner. Berechnung der natürlichen Linienbreite auf Grund der Dirac'schen Lichttheorie. *Zeitschrift für Physik* **63**(1-2), 54–73 (1930).

[73] M. Florian, C. Gies, P. Gartner and F. Jahnke. Improved antibunching by using high-excitation pulses from a single semiconductor quantum dot – a theoretical study. *J. Opt. Soc. Am. B* **29**(2), A31 (2012).

[74] R. Ferreira and G. Bastard. *Capture and Relaxation in Self-Assembled Semiconductor Quantum Dots*. 2053–2571. Morgan & Claypool Publishers (2015).

[75] P. Farrell, N. Rotundo, D. H. Doan, M. Kantner, J. Fuhrmann and T. Koprucki. *Mathematical Methods: Drift-Diffusion Models.* In J. Piprek (editor): *Handbook of Optoelectronic Device Modeling and Simulation*, Vol. 2, Ch. 50, 731–769, CRC Press Taylor & Francis Group (to appear 2017).

[76] D. L. Scharfetter and H. K. Gummel. Large-signal analysis of a silicon read diode oscillator. *IEEE T. Electron Dev.* **16**(1), 64–77 (1969).

[77] M. Bessemoulin-Chatard. A finite volume scheme for convection–diffusion equations with nonlinear diffusion derived from the Scharfetter–Gummel scheme. *Numer. Math.* **121**(4), 637–670 (2012).

[78] T. Koprucki, N. Rotundo, P. Farrell, D. H. Doan and J. Fuhrmann. On thermodynamic consistency of a Scharfetter–Gummel scheme based on a modified thermal voltage for drift-diffusion equations with diffusion enhancement. *Opt. Quant. Electron.* **47**(6), 1327–1332 (2014).

[79] M. Kantner and T. Koprucki. Numerical simulation of carrier transport in semiconductor devices at cryogenic temperatures. *Opt. Quant. Electron.* **48**(12), 543 (2016).

[80] S. Selberherr. Low temperature MOS device modeling. In *Proc. of the 172nd Meeting of the Electrochem. Soc.*, Vol. 88-9, 70–86, Honolulu (1987).

[81] D. M. Richey, J. D. Cressler and R. C. Jaeger. Numerical simulation of SiGe HBT's at cryogenic temperatures. *J. Phys. IV France* **4**(C6), C6–127–C6–32 (1994).

[82] C. Gardiner and P. Zoller. *Quantum Noise: A Handbook of Markovian and Non-Markovian Quantum Stochastic Methods with Applications to Quantum Optics*, Vol. 56 of *Springer Series in Synergetics*. Springer (2004).

[83] P. Michler. *Quantum Dot Single-Photon Sources*, Ch. 6, 185–225. In Michler [4] (2009).

[84] A. J. Bennett, R. B. Patel, A. J. Shields, K. Cooper, P. Atkinson, C. A. Nicoll and D. A. Ritchie. Indistinguishable photons from a diode. *Appl. Phys. Lett.* **92**(19), 193503 (2008).

[85] V. Zwiller, T. Aichele and O. Benson. Quantum optics with single quantum dot devices. *New J. Phys.* **6**, 96 (2004).

[86] N. B. Abdallah, F. Méhats and N. Vauchelet. Analysis of a drift-diffusion-Schrödinger–Poisson model. *C. R. Math.* **335**(12), 1007–1012 (2002).

[87] M. Baro, H. Neidhardt and J. Rehberg. Current coupling of drift-diffusion models and Schrödinger–Poisson systems: Dissipative hybrid models. *SIAM J. Math. Anal.* **37**(3), 941–981 (2005).

[88] T. Grasser, T.-W. Tang, H. Kosina and S. Selberherr. A review of hydrodynamic and energy-transport models for semiconductor device simulation. *P. IEEE* **91**(2), 251–274 (2003).

[89] V. Sverdlov, E. Ungersboeck, H. Kosina and S. Selberherr. Current transport models for nanoscale semiconductor devices. *Mat. Sci. Eng. R.* **58**(6), 228–270 (2008).

[90] A. Jüngel. *Transport Equations for Semiconductors*, Vol. 773 of *Lecture Notes in Physics*. Springer: Berlin Heidelberg (2009).

[91] R. H. Dicke. Coherence in spontaneous radiation processes. *Phys. Rev.* **93**(1), 99 (1954).

[92] G. Lindblad. Completely positive maps and entropy inequalities. *Comm. Math. Phys.* **40**(2), 147–151 (1975).

[93] H. Spohn. Entropy production for quantum dynamical semigroups. *J. Math. Phys.* **19**(5), 1227–1230 (1978).

[94] V. Palankovski and R. Quay. *Analysis and Simulation of Heterostructure Devices*. Computational Microelectronics. Springer: Vienna (2004).

[95] T. T. Mnatsakanov, M. E. Levinshtein, L. I. Pomortseva and S. N. Yurkov. Universal analytical approximation of the carrier mobility in semiconductors for a wide range of temperatures and doping densities. *Electronic and Optical Properties of Semiconductors*, **38**(1), 56–60 (2004).

[96] N. F. Mott. Metal-insulator transition. *Rev. Mod. Phys.* **40**(4), 677–683 (1968).